This manuscript is a post print of a paper accepted in Bulletin of Volcanology in February 2024.

Tephra dispersal and composition reveal the explosive onset of a large basaltic fissure eruption: Timanfaya, Lanzarote, 1730–1736 CE

James K. Muller[1,2] and Marc-Antoine Longpré[1,3*]

[1]School of Earth and Environmental Sciences, Queens College, City University of New York, Queens, NY 11367, USA
[2]Scripps Institution of Oceanography, University of California San Diego, La Jolla, CA 92093, USA
[3]Earth and Environmental Sciences, The Graduate Center, City University of New York, New York, NY 10016, USA

*Corresponding author at: School of Earth and Environmental Sciences, Queens College, City University of New York, Queens, New York 11367, USA.
E-mail address: mlongpre@qc.cuny.edu (M.-A. Longpré)

ABSTRACT

Basaltic fissure eruptions are chiefly characterized by sizable emissions of lava flows and volcanic gases, posing significant hazards. However, such eruptions may be punctuated by explosive episodes, which are comparatively poorly understood but may have important volcanic hazard and environmental implications. The 1730–1736 CE Timanfaya eruption on Lanzarote, Canary Islands, is a large basaltic fissure eruption characterized by a marked temporal–compositional trend from early basanite to late tholeiite lavas, but little is known on its associated pyroclastic deposits and potential environmental repercussions. Here we report field and geochemical data from tephra deposits to reconstruct the temporal evolution of eruptive style and provide constraints on the impact of the Timanfaya eruption. Stratigraphic sections demonstrate the pulsatory nature of explosive activity during the eruption and the wide dispersal of the tephra blanket, for which a minimum bulk volume of ~0.44 km^3 is derived. Isopleth data from a basal tephra layer tied to an early, particularly powerful eruption pulse suggest that eruption columns lofted to ≥8 km altitude. We find that nearly all distal tephras are characterized by low SiO_2 content and high incompatible trace element concentrations that only match the compositions of tephras sourced from vents active in the eruption's initial phase. This implies that the most violent explosive activity, responsible for the emplacement of the tephra blanket, was restricted to the first few months of the eruption, after which eruptive style was dominated by lava effusion and mild cone-building Strombolian activity. We argue that explosive activity at Timanfaya was similar to that of the 1783–1784 CE Laki and 2021 Cumbre Vieja eruptions and highlight the explosive potential of mafic volcanism in the Canary Islands. Trace element proxies for volatile elements suggest that early basanitic magmas were particularly rich in CO_2, sulfur, and chlorine. We infer that the Timanfaya eruption released 65–388 Tg CO_2, 9–23 Tg S, and 2–9 Tg Cl to the atmosphere; however, ice core evidence indicates that little to no sulfur reached Greenland, consistent with tropospheric transport of gas emissions. Some climate proxy records show anomalies that may be related to Timanfaya, but the environmental impact of the eruption beyond Lanzarote remains unclear.

KEYWORDS: Basaltic fissure eruptions, eruptive style, tephra stratigraphy, Lanzarote, Timanfaya

INTRODUCTION

Large basaltic fissure eruptions pose significant hazards, mostly through massive emissions of lava flows and volcanic gases that can negatively impact the environment. Recent examples include the 2014–2015 Holuhraun eruption, Iceland (Gudmundsson et al., 2016), and the 2018 lower East Rift Zone eruption of Kīlauea volcano, Hawai'i (Neal et al., 2019), but perhaps the best-known case is the 1783–1784 CE Laki eruption, in Iceland (Thordarson & Self, 1993, 2003). The Laki eruption produced a huge lava flow field, some 599 km^2 in area and 14.7 km^3 in volume, from a 27-km-long fissure and it released ~304 Tg CO_2,122 Tg SO_2, 7 Tg HCl and 15 Tg HF to the atmosphere, leading to adverse environmental effects particularly acute in Iceland but felt across the Northern Hemisphere (Hartley et al., 2014; Thordarson et al., 1996; Thordarson & Self, 2003). Along with lava effusion and gas emissions, basaltic fissure eruptions may also include explosive phases, producing extensive tephra fall as an additional hazard. In Iceland, for instance, five out of 13 large basaltic fissure eruptions in historical time are associated with widespread tephra layers (e.g., Thordarson & Larsen, 2007). At Laki, eruption plumes reaching maximum heights of 6–13 km produced a tephra blanket of 0.76 km^3 in volume (0.4 km^3 dense rock equivalent — DRE) (Thordarson & Self, 1993). The explosive phases of basaltic fissure eruptions may span Hawaiian, Strombolian, violent Strombolian, phreatomagmatic, and even Plinian eruption styles (Thordarson & Larsen, 2007; Valentine & Gregg, 2008; Walker et al., 1984), but have received comparatively little attention, perhaps because they commonly represent a small volumetric fraction of the eruptive products. Yet, the intensity of these explosive phases control tephra fall hazards and, in part, the climate consequences of a given eruption, because climate-impacting volcanic gases have a much longer atmospheric residence time if injected above the tropopause by tall plumes (e.g., Robock, 2000). A better understanding of explosive activity associated with basaltic fissure eruptions also has important implications for extrapolation to much larger flood basalt eruptions (e.g., Brown et al., 2014; Glaze et al., 2017; Self et al., 2006).

The 1730–1736 CE Timanfaya eruption, on the island of Lanzarote in the Canary Islands, ranks second to Laki among the largest basaltic fissure eruptions of the last millennium globally. This long-duration event (2055 days) produced a complex lava flow field covering 146 km^2 and at least 2.2–3.7 km^3 in volume, destroying 26 villages and forcing the exodus of much of the island's inhabitants (Carracedo et al., 1990, 1992; Carracedo & Rodríguez Badiola, 1991; Longpré & Felpeto, 2021). Timanfaya lavas are characterized by their high MgO content, up to ~17 wt.%, and a temporal–compositional trend from early basanites to late tholeiites (Carracedo et al., 1990, 1992), which attracted substantial scientific attention (Gómez-Ulla et al., 2017, 2018; Lundstrom et al., 2003; Reiners, 2002; Sigmarsson et al., 1998; Thomas et al., 1999). The eruption also produced significant explosive activity, as attested by historical records (Carracedo, 2014; Longpré & Felpeto, 2021; Romero, 2003). However, besides work focusing on post-eruptive sedimentary processes (Criado et al., 2013), the resulting tephra blanket, the most conspicuous part of which forms La Geria, a wine-producing valley (Troll et al., 2017), has not yet been studied in detail.

Recent work by Sharma et al. (2024) — based on sulfur concentration in melt inclusions, as well as incompatible element proxies for magmatic sulfur — suggests that the Timanfaya eruption released ~42 Tg SO_2 (21 Tg S), about a third of Laki's sulfur output. However, ice core

records show limited evidence for volcanic sulfur deposition in the early 1730's (e.g., Sigl et al., 2015; Zielinski, 1995), and so very little to none of Timanfaya's sulfur appears to have reached Greenland (Sharma et al., 2024). In addition, while there are some mentions of environmental effects possibly associated with Timanfaya in the literature (e.g., D'Arrigo et al., 2009), little is known about the impact of the eruption beyond Lanzarote.

In this paper, we report the results of fieldwork and geochemical analyses of tephra deposits of the Timanfaya eruption, with the goals of reconstructing its eruption style over time and improve constraints on its impact. After summarizing relevant background information and methods for context, we document the wide dispersal of tephra and outline estimates of tephra volume and eruption column heights. We then describe the composition of tephra samples, and, based on the distinct chemical fingerprints of the eruptive phases, correlate the distal tephra blanket to its source vents. The results indicate that explosive activity was largely restricted to the initial phase of the eruption. Finally, we draw comparisons with other basaltic eruptions and discuss constraints on volatile outputs and the evidence for a potential environmental impact of the eruption.

BACKGROUND

Geologic context

The Canary Islands are intraplate volcanic edifices located off the coast of Morocco in the eastern Atlantic Ocean and built on Jurassic oceanic crust (Schmincke et al., 1998). The age of the oldest subaerial volcanic rocks on the seven main islands shows a broad and discontinuous east–west progression, from 20 Ma at Fuerteventura to 1.1 Ma at El Hierro (e.g., van den Bogaard, 2013; Zaczek et al., 2015, and references therein). Lanzarote is the easternmost island of the archipelago (Fig. 1) and comprises two shield complexes — Famara (10.2 to 3.8 Ma) in the north and Los Ajaches (15.5 to 12.3 Ma) in the south (Coello et al., 1992; Perez-Torrado et al., 2023). After an apparent hiatus of 1–2 million years, during which extensive erosion blunted Lanzarote's topography, rejuvenated volcanism in the Pleistocene produced multiple fissure eruptions, forming northeast–southwest alignments of cinder and tuff cones. La Quemada, Corona, and Los Helechos volcanoes, located in the northeastern part of the island and dated at ~21 ± 6.5 ka, may represent the youngest prehistoric eruption on the island (Carracedo et al., 2003). Of the 14 historical eruptions in the Canary Islands since 1500 CE, including the 2021 Cumbre Vieja eruption on La Palma, two took place on Lanzarote, in 1730–1736 and 1824 (Longpré & Felpeto, 2021).

The Timanfaya eruption

Previous work summarized herein (see Longpré & Felpeto, 2021 for details) provides important context on the chronological development of the Timanfaya eruption and the compositional evolution of erupted lavas. Carracedo and Rodríguez Badiola (1991) and Carracedo et al. (1990, 1992) used geologic mapping, analysis of historical sources, and bulk lava compositions to reconstruct the eruption, which was divided into five phases involving ten principal emission centers. Figure 1 shows the location of these main vents and their respective lava flows, as well as a summary eruption chronology, based on these works, whereas Figure 2 illustrates the temporal–compositional evolution of erupted lavas using published data for which

samples were tied to specific eruptive episodes (Carracedo et al., 1990; Gómez-Ulla et al., 2017; Thomas et al., 1999).

Phase 1 of the eruption built three successive cinder cones — Caldera de los Cuervos (1–19 September 1730), Caldera de Santa Catalina (10–31 October 1730) and Pico Partido (10 October 1730 to January 1731) — and a large lava flow field reaching the northwest coast (Fig. 1). These flows buried several villages and historical sources also clearly indicate that these early eruptive episodes involved considerable explosive activity. Thick lapilli and ash accumulations damaged roofs and spoiled farmland (Carracedo, 2014; Longpré & Felpeto, 2021; Romero, 2003). Eruptive products at Caldera de los Cuervos are basanites characterized by an abundance of peridotite xenoliths, extremely high MgO (14.1–16.8 wt.%) contents and high incompatible element concentrations, such as potassium (1.5 wt.%) (Fig. 2). Lavas of Pico Partido and Caldera de Santa Catalina also contain peridotite xenoliths and are mostly alkali basalts; samples generally show high MgO (7.8–13.5 wt.%) and incompatible element concentrations (0.6–1.3 wt.% K_2O), though values are lower than at Caldera de los Cuervos.

Following an apparent hiatus of a few weeks, Phase 2 of the eruption took place in at least four distinct stages between March and July 1731, at Montañas del Señalo, located just to the south of Pico Partido. Flows emitted from Montañas del Señalo stretched north near to the large prehistoric tuff cone of Caldera Blanca and southwest towards the towns of Uga and Yaiza. These lavas are xenolith-poor and straddle the compositional divide between alkali and tholeiitic basalt. Their MgO and K_2O contents range from 9.0 to 10.3 wt.% and 0.6–0.8 wt.%, respectively.

Phase 3 of the eruption began at the end of June 1731 as the activity shifted at least 12 km to the west, initially below sea level and then onshore at the small Volcán El Quemado, which is located ~1 km from the coast and produced a minor alkali basalt lava flow (10.7–11.4 wt.% MgO, 0.7–0.9 wt.% K_2O). The focus of the activity subsequently migrated to the east, forming Montaña Rajada and then Calderas Quemadas, a group of four closely-spaced cinder cones. Lavas from these vents comprise the westernmost expanses of the lava flow field, including along the coastline near to the town of El Golfo. They are alkali to tholeiitic basalts (8.9–11.0 wt.% MgO, 0.6–0.9 wt.% K_2O), with the exception of one sample reported by Thomas et al. (1999) and assigned to Montaña Rajada that is similar to Caldera de los Cuervos lavas.

At this point, the strong impact of the eruption on the island's infrastructure and farmland led to massive exodus of the inhabitants, and as a result contemporary information becomes very scant (Fig. 1b). Based on mapping (Carracedo & Rodríguez Badiola, 1991), Phase 4 of the eruption, beginning in early 1732 and possibly persisting until early 1736, is inferred to have focused at Montañas del Fuego, a large and complex cluster of overlapping cinder cones. Abundant lavas from Montañas del Fuego flowed towards the northwest and southwest, comprising much of present-day Timanfaya National Park. These lavas are alkali to tholeiitic basalt, with 7.9–11.2 wt.% MgO and 0.6–0.9 wt.% K_2O, except one sample from Thomas et al. (1999) which is a high-MgO basanite.

The fifth and final eruptive phase took place at Montaña de Las Nueces and Montaña Colorada, 5 km east of Montañas del Fuego, but the timing of its onset is uncertain. It was originally deduced that activity at Montaña de las Nueces had occurred from mid-March to early April 1736, producing a large pāhoehoe lava flow that reached the coast near the town of Arrecife to the east (Carracedo et al., 1992; Solana et al., 2004). However, a reassessment of

historical archives by Pallarés Padilla (2007) suggests that lava flows emitted from this vent already threatened the town's port by February 1733. If so, Phase 5 would have begun at least three years earlier than formerly thought. The final emission center of the Timanfaya eruption is Montaña Colorada, which may have been active for only two weeks ending on 16 April 1736. This cone emitted lavas that flowed north, falling just short of reaching the coast, and produced a significant lapilli field on its south flank. Phase 5 lavas are mostly tholeiitic basalts, showing among the lowest MgO (8.3–11.5 wt.%) and incompatible trace element concentrations (0.6–0.7 wt.% K_2O) of the entire eruptive sequence (Fig. 2). While Montaña de las Nueces lavas are xenolith-poor, Montaña Colorada lavas feature abundant peridotite and silicic xenoliths of metasedimentary origin (Aparicio et al., 2006).

Occurring nearly a century after the Timanfaya eruption, the 1824 eruption was much smaller and shorter in duration (spanning 87 days). It formed three cinder cones, Volcán de Tao, Volcán Nuevo del Fuego, and Volcán de Tinguatón, which are aligned ENE–WSW and spaced by a total of 14 km, and small lava flow fields mostly atop 1730–1736 lavas (Fig. 1) (Longpré & Felpeto, 2021; Romero, 2003). The 1824 lavas are high-MgO basanites, similar in composition to samples from Caldera de los Cuervos and Pico Partido (Fig. 2).

METHODS

Tephrostratigraphy and sampling

The stratigraphy of Timanfaya tephra was documented at 31 localities across Lanzarote (Figs. 3, 4, S1, Table S1). Following a modified grid system, we generally selected sites that were ≥10 m away from lava flows on terrain as flat as possible to minimize syn- and post-emplacement deposit reworking effects (e.g., Brown et al., 2015) and that showed no to minimal evidence of anthropogenic disturbance. The latter was a significant limitation in field site selection as large swaths of the tephra blanket has been partially reworked to grow vines (Troll et al., 2017). At each selected suitable locality, we dug trenches until reaching the base of the tephra deposit, typically marked by an orangey paleosol, sediments or weathered, pre-18th century lava flows. Graphic logs (Figs. 3, S1) were constructed for each site, recording the thickness, componentry, grain size and mineralogy of individual tephra beds, using the terminology and classification scheme of White and Houghton (2006). Maximum clast size for each tephra layer was taken as the average of the 5 largest clasts.

Samples were taken at high stratigraphic resolution, from each individual bed identified and deemed in situ (from the lack of evidence of reworking, e.g., cross-bedding) within each trench (Fig. S1). At some locations, the bottom and top of particularly thick beds were sampled. We refer to samples collected from trenches, which are all located ≥750 m away from the eruptive fissure, as *distal tephras*, whereas *vent tephras* correspond to samples collected directly from the flanks of the main cinder cones, thus representing the late stage of individual eruptive episodes.

Density measurements

The density of tephra deposits was estimated in the laboratory. Individual representative lapilli were weighed in air, subsequently sealed in Parafilm (e.g., Houghton & Wilson, 1989) and

submerged in water to obtain their volume by displacement. We assumed that the Parafilm added negligible volume.

The density of lava blocks was measured directly in the field using Archimedes' principle and the methodology of Kueppers et al. (2005). To obtain a representative lava density distribution, we selected blocks of 'a'ā flow tops and cores as well as of pāhoehoe flows that averaged 20–40 cm length on any given side. The average bulk lava flow density was then determined using the estimated proportions of flow typologies, as detailed in the Supplementary Methods and Table S2.

X-ray fluorescence

The major and selected trace element composition of bulk rock samples of a set of 15 vent tephras and ten distal tephras was analyzed by X-ray fluorescence (XRF) on a Thermo ARL Advant'XP+ XRF sequential spectrometer at Washington State University, based on established protocols (Johnson et al., 1999). Analyses of duplicate samples and of an in-house standard (COS-M-50; Longpré et al., 2014) were used to confirm the high precision and accuracy of the data (see Table S3 for details).

Electron probe microanalysis

The major and volatile (S, Cl) element concentrations in matrix glasses of 15 vent and 74 distal tephras were measured with a JEOL 8900 electron microprobe at McGill University, using a 15 kV accelerating voltage, 10 nA current, and 15 μm beam size. Sodium was analyzed first to minimize loss by volatilization. Peak/background counting times were 20/10 s for all elements, except Cl (60/30 s) and S (120/60 s). The instrument was calibrated using synthetic and natural standards, including the Makahoupi basaltic glass standard USNM 113498 A-99 (Jarosewich, 2002) for Si, Ti, Mg, Fe, Al, Ca, and Na and KE-12 obsidian glass (Devine et al., 1995a) for K. Data quality was monitored by replicate analyses of VG-2 (USNM 111240-52) (Jarosewich, 2002) and P1326-2 (Stix et al., 1995) basaltic glasses during our analytical session (Table S3).

Inductively coupled plasma mass spectrometry

Bulk rock samples of four selected vent tephras were analyzed for trace element concentrations by inductively coupled plasma mass spectrometry (ICP-MS) on an Agilent 7700 quadrupole instrument using a routine method at the GeoAnalytical Lab of Washington State University, which has a long-term relative precision (1σ) better than 5% for rare earth elements and 10% for other elements (Knaack et al., 1994). As for XRF, one of our samples was run in duplicate, showing reproducibility better than 3% relative for all elements, and standard COS-M-50 was also run to check accuracy, with data agreeing with preferred values within 10% relative (Table S3).

Matrix glasses of 15 vent and 58 distal tephras were analyzed by laser ablation ICP-MS for trace element abundances at Lamont-Doherty Earth Observatory of Columbia University, using an ESI New Wave UP 193 FX excimer laser coupled to a VG ExCell quadrupole mass spectrometer. Samples were ablated in an Ar-He mixture at a flow rate of ~0.6 mL min^{-1} and 1.6 mL min^{-1}, respectively, using the laser in spot-drill mode at 10 Hz and 90% power, giving a mean energy density of 11.3 J cm^{-2} and irradiance of 2.26 GW cm^{-2}. Spectra were collected by

peak-hopping; dwell times were 10 ms for all analytes, of which ^{43}Ca was used for normalization. Beam sizes of 50 and 75 μm were used for unknowns and standard glasses (BCR-2G, BIR-1G, and BHVO-2G), respectively. Counting times were 60 s on background and 60 s on peak. Calibration curves defined by the standards were linear ($R^2 \geq 0.99$). The high precision and accuracy of the data were confirmed by replicate analyses in-house standard P1326-2 (Table S3). Data reduction was completed using the LasyBoy macro (v. 3.77f; J. Sparks, Boston University), and GeoReM preferred values (Jochum & Nohl, 2008) for the compositions of USGS glass standards.

RESULTS

Field observations and stratigraphy

Cinder cones associated with the Timanfaya eruption are built by both agglutinate spatter and loose pyroclasts (see also Kervyn et al., 2012), which are dominantly gray to black, glassy and scoriaceous lapilli and ash. Tephra at Caldera de los Cuervos is characterized by a blueish, pseudo-iridescent sheen, whereas that at Montaña Colorada is distinct, consisting in part of a light golden brown, frothy scoria. Clasts are generally olivine-phyric, with individual olivine crystals typically up to 1 mm in size. Larger crystal clots, frequently ≥1 cm across, are common and likely represent disaggregated peridotite xenoliths. Such xenoliths attain dimensions of ~30 cm in the crater walls of Caldera de los Cuervos and occur as brick-sized bombs on the flanks of Pico Partido.

At locations away from the eruptive fissure, fresh tephra most commonly occurs sandwiched between, at its base, a conspicuous orangey paleosol comprising volcaniclastic and aeolian sediments that formed over ~40 ky (Criado et al., 2013; Jahn & Stahr, 1996; von Suchodoletz et al., 2008) and, at its top, a brownish, poorly sorted layer of weathered lapilli and sediments (Figs. 3, S1), sometimes displaying irregular laminations. We interpret this capping layer to be reworked tephra and sediment that formed from colluvial processes and/or anthropogenic activity, and we excluded it from our analysis. The fresh, laterally extensive tephra, however, almost certainly derives from the Timanfaya eruption, consistent with radiocarbon ages bracketing it between the 14th and 19th century (Criado et al., 2013). Selected representative stratigraphic sections through this deposit are shown in Figure 3, with the location of corresponding field sites (LZ-#) shown in Figure 4 as a red number. All sections along with the stratigraphic position of samples are provided in Figure S1. Individual sections typically show multiple continuous beds most often delineated by abrupt changes in grain size, which generally ranges from coarse ash to medium lapilli, although coarse lapilli with maximum clast size up to 5 cm are found at sites closest to the fissure (e.g., LZ-12, -24, -29) (Figs. 3, 4, S1). Beds at the base of sections are often the coarsest and thickest (Figs. 3, 4, S1). The grain size and thickness of individual beds tend to decrease up-section, while sorting generally increases. Individual beds are commonly reversely graded.

The deposit is dominated by similar gray to black, glassy clasts (Fig. 3b). However, clasts from beds near the base of sections commonly exhibit a pseudo-iridescent sheen, reminiscent of Caldera de los Cuervos vent tephra. In addition, at several localities (e.g., LZ-4, -15, -19, -27), we identified horizons rich in Pele's hair, as observed in the Laki tephra (Thordarson & Self, 1993) (Figs. 3, S1), suggesting rapid tephra accumulation rates allowing

preservation of these delicate fragments. Peridotite lithics as well as white to gray pumice-like clasts are also occasionally found, the latter resembling “xeno-pumices” commonly co-erupted with mafic magma in the Canaries and thought to represent melted silicic sediments (e.g., Aparicio et al., 2006; Carracedo et al., 2022; Troll et al., 2012) (Figs. 3, S1). Minor lithological variation occurs in the uppermost strata deemed in situ of some trenches, in any of three ways: (1) pyroclasts may culminate in a thin (a few cm) layer of light brown, frothy scoria similar in appearance to that found on the summit of Montaña Colorada (e.g., LZ-4, -15, Fig. 3c); (2) small (≤1 cm) light-colored lithic clasts resembling metasedimentary xenoliths from Montaña Colorada may increase in abundance (e.g., LZ-4, -24); and (3) at three localities (LZ-24, -27, 28) deposits include a thin layer of accretionary lapilli. We also observed a horizon containing plant roots in the upper part (~10 cm below the section top) of two sections, LZ-4 and LZ-15, which both exceed 1 m thickness. The origin of these roots is unclear, but they may mark the interface between Timanfaya tephras and locally preserved, thin deposits from the 1824 eruption.

The total thickness of the tephra blanket at the studied sites is shown in Figure 4a. Tephra thicknesses are greatest in the area of La Geria, just south of the lava flow field and the vents from Phase 1 of the eruption. We measured a maximum thickness of 1.8 m at site LZ-12, where, however, the base of the deposit could not be reached (as at the neighboring LZ-29 site). The tephra blanket may reach a thickness of 3–4 m in parts of La Geria, according to cross-section exposures along gullies (Sharma, 2005). At Caldera de Gaida ~5 km south of the fissure (locality LZ-4), the tephra exceeds 1 m thickness. At our most distal location (LZ-3) — at an incised hillside near Guatiza ~20 km northeast of Montaña Colorada, corresponding to locality 5 of Criado et al. (2013) — the fine tephra layer is 10 cm thick. Overall, these data confirm the wide dispersal of the Timanfaya pyroclasts, consistent with the data of Criado et al. (2013) as well as with historical sources reporting ashfall across much of Lanzarote and as far as neighboring Fuerteventura (Carracedo, 2014; Romero, 2003). Greater thicknesses south of the fissure likely reflect dominant northerly winds (Fig. 4b inset), although exposures north of the fissure may be underrepresented due to the lava flow field. We note that tephra dispersal by northerly winds also appears to commonly affect the morphology of cinder and tuff cones on Lanzarote, including Caldera de los Cuervos, with southern crater rims typically showing higher elevations than northern crater rims (Kervyn et al., 2012).

Tephra volume

Based on tephra thickness data, we used a regularized spline contouring method (Engwell et al., 2015) to construct 5 isopachs — at thicknesses of 10, 20, 40, 80, and 160 cm — in an effort to balance precision against the potential of overfitting the data (Fig. 4a, Supplementary Methods). The total area enclosed within each isopach was calculated using ArcGIS. In Figure 5, tephra thickness is plotted against the square root of area, which effectively normalizes the deposit to an ideal, concentric form and allows calculating its volume by integrating under the curve (Pyle, 1989). Using the AshCalc software (Daggitt et al., 2014), we fitted the isopach data with a single exponential segment, which yields a bulk tephra blanket volume of 0.44 km^3. We take this value to represent a relatively robust minimum estimate, as replicate analyses using different methods, i.e., multi-segment exponential thinning and Weibull thinning (Bonadonna & Costa, 2012), agree within ~10% (see Supplementary Methods).

However, our data do not allow constraining the 1 cm isopach, which may contain a significant fraction of the deposit (Bonadonna & Costa, 2012).

The above figure also excludes the proximal tephra volume contained within the cones. On the basis of idealized cone volume calculations with cone height and cone diameter measured in ArcGIS, we estimate the main ~15 cones constructed over the course of the eruption to sum to ~0.1 km^3. In comparison, Kervyn et al. (2012) obtained 0.07 km^3 for Timanfaya cones (M. Kervyn, personal communication, 2020).

Our density measurements on five individual pyroclasts (two from vent tephras, three from distal tephras) yield 1,260 ± 240 kg/m^3 (Table S2). While our sample size is small, our values agree well with the mean tephra blanket density for the 2021 Cumbre Vieja eruption (1,200 ± 120 kg/m^3, Bonadonna et al., 2022) and thus likely represent a reasonable approximation for the Timanfaya tephra blanket density. Using the above figures, we convert the bulk volume of the tephra blanket to 0.20 km^3 DRE. In comparison, our field measurements of lava block density (n = 28) yield a weighted mean of 2,120 kg/m^3 (Table S2). As the density of cone-building agglutinated spatter and lapilli is likely between that of lavas and loose pyroclasts (i.e., in the range 1,260–2,120 kg/m^3), we deduce a DRE cone volume between 0.03 and 0.08 km^3. Hence the minimum combined proximal and distal tephra volume is 0.51–0.54 km^3 (0.23–0.28 km^3 DRE).

Eruption column height

The maximum grain size of tephra fall deposits is a function of distance from the vent and the eruption explosivity, and it may be used to estimate eruption column height (e.g., Pyle, 1989) — a parameter that is ill-constrained for historical Canary Island eruptions (Longpré & Felpeto, 2021). However, as attested by multiple beds of varying grain size in stratigraphic sections (Fig. 3), the Timanfaya eruption occurred in multiple pulses, which is common for cinder cone-producing eruptions (e.g., Pioli et al., 2008). Using isopleths for the total tephra deposit would thus yield erroneous (overestimated) column height estimates. In this context, our approach to constrain maximum eruption column height focuses on the distinctive basal lapilli bed, which is present in several trenches and likely tied to Caldera de los Cuervos based on componentry (and composition, as will be demonstrated subsequently) (Fig. 3). We take this bed to represent a particularly vigorous eruption pulse near the eruption's inception, as it is commonly the thickest and coarsest at any given locality.

In Figure 4b, two sets of isopleths are thus shown — one for the full deposit, the other for the basal bed only. Contouring was performed as described for isopachs. The number of data points for the basal bed is restricted (eight), likely causing contouring artifacts. Nevertheless, basic inferences can be made. The east–west extent of the 10 mm isopleth indicates that early explosive activity, affected an area almost as large as that of the cumulative whole of the Timanfaya eruption. Indeed, 10-mm lapilli reached more than 10 km from the vent. Using a MATLAB implementation (Biass et al., 2015) of the model of Carey and Sparks (1986), we utilized our isopleth data to constrain eruptive plume height above the crater (~320 m above sea level for Caldera de los Cuervos, Longpré & Felpeto, 2021). Based on the 20 mm isopleth and the measured bulk tephra density (1,260 kg/m^3, Table S2), we obtain eruption columns reaching 8 km, which is taken as a minimum value as eruption plumes may reach beyond their level of neutral buoyancy (Carey & Sparks, 1986).

Tephra composition

All geochemical data on our Timanfaya samples are reported in Table S4. The bulk rock composition of vent tephras shows ranges of 43.0–50.9 wt.% SiO_2 and 4.7–3.3 wt.% total alkalis (Fig. 6a), closely replicating the early basanite to late tholeiite trend previously established based on lava samples (Fig. 2a) (Carracedo et al., 1990). Tephras from Phase 1 vents are highly enriched in incompatible trace element concentrations, also in line with published data (Fig. 7a). In addition, trace element ratios, such as Zr/Nb, of vent samples correlate well with those of corresponding lava samples, confirming the lava–source vent associations defined by Carracedo et al. (1990) (Fig. 6c).

The matrix glasses of vent tephras (43.4–53.0 wt.% SiO_2, 6.4–3.6 wt.% total alkalis) are broadly similar to their respective bulk rocks, also shifting from basanitic to tholeiitic compositions over the eruption sequence (Figs. 6b, 8a). Glasses show much lower MgO contents (5.0–6.2 wt% MgO, vs. 9.4–14.0 wt% in the bulk rocks, Fig. 6d), however, reflecting the olivine-rich crystal cargo of the bulk rocks (see also Gómez-Ulla et al., 2017). Importantly, as for bulk rocks, incompatible element concentrations vary substantially in glasses from different eruption phases, with samples from Caldera de los Cuervos, Pico Partido and Caldera de Santa Catalina consistently displaying the most enriched compositions (Fig. 7b). Glasses from these earliest eruptive episodes also exhibit negative high field strength element (HFSE, e.g., for Zr and Hf) anomalies, which are not observed in samples from subsequent eruptive phases. Ratios of highly incompatible to moderately incompatible elements provide additional useful proxies for the degree of enrichment. For example, we find that Nb/Y ratios are up to a factor of two higher in Phase 1 basanitic tephras relative to Phase 5 tholeiitic tephras (Fig. 8b). Finally, vent tephra glasses are also characterized by decreasing chlorine concentrations over the eruptive sequence, from 900 ppm at Caldera de los Cuervos to 300 ppm at Montaña Colorada (Fig. 9a). Sulfur concentrations, on the other hand, are generally low to below detection limit of our EPMA setup (i.e., <140 ppm, Table S4), due to effective degassing.

For distal tephras, limited bulk rock data are consistent with vent tephra compositions, with SiO_2 contents increasing from 43.4 to 48.0 wt.% as total alkalis decrease from 4.5 to 3.6 wt.% (Fig. 6a). However, more abundant EPMA and LA-ICP-MS data on matrix glasses allow a fuller characterization of distal tephra compositions and comparison with vent tephras. We find that, while distal tephra glasses overall span a slightly wider compositional range than those of vent samples, most are characterized by low SiO_2, high incompatible element concentrations, high chlorine and negative HFSE anomalies (Figs. 6b, 7b, 8, 9). These characteristics strongly resemble the composition of Phase 1 vent tephras.

Distal tephra–source vent correlation

We assigned each distal tephra sample to its likeliest source vent by exploiting the distinct signatures of eruptive episodes in P_2O_5–SiO_2 and Nb/Y–SiO_2 spaces (Fig. 8). In this approach, we used the Euclidean distance formula to solve for the distance between each distal sample and all the vent samples — the shortest distance obtained then ties each distal tephra to its source vent. Our method assumes that the vent tephra samples, which record the late stage of each episode, are representative of their respective episode and thus that intra-episode compositional zoning was limited. While some intra-episode variability is suggested by the wider compositional range exhibited by distal tephras, their clustering in groups in several chemical discrimination diagrams (e.g., Figs. 7b, 8a, 9b) supports our assumption. Limited intra-episode zoning is also consistent with the similarity of lava samples associated with each episode (Fig. 2). The resulting distal tephra–source vent associations, which are very similar for P_2O_5–SiO_2 and Nb/Y–SiO_2, are listed in Table S5 and allow reconstructing the stratigraphic sequence at each of our trench sites (Fig. 3). In cases where correlations based on P_2O_5–SiO_2 and Nb/Y–

SiO_2 differed, we used the P_2O_5–SiO_2 result, as data have a better precision and are available for more samples. Our reconstructions are broadly (but not always perfectly) consistent with the eruption timeline of Carracedo et al. (1990; 1992) (Fig. 1b). For instance, the section at site LZ-4 features basal Caldera de los Cuervos tephra successively overlain by Pico Partido and Caldera de Santa Catalina tephra, with a thin cap of Montaña de las Nueces tephra (Fig. 3), which concords with the established eruptive sequence. In contrast, at site LZ-27, for example, tephra best matched to Montañas del Fuego is sandwiched between beds correlated to Caldera de Santa Catalina and Pico Partido (Fig. 3), which is at odds with the known eruption timeline. Such discrepancy could be explained by thus far unrecognized compositional zoning within individual eruptive phases/episodes and/or underappreciated complexities in the eruptive sequence. Nevertheless, the key observation of this exercise remains: 38% of distal tephras are correlated to Caldera de los Cuervos, 12% to Pico Partido and 38% to Caldera de Santa Catalina, with the balance mostly matched to Montañas del Fuego (8%). Therefore, unless they have all been reworked or eroded, which appears highly unlikely, transitional to tholeiitic tephra compositions from other episodes largely did not reach our field sites.

DISCUSSION

An explosive onset at Timanfaya

The above results confirm that the bulk of the tephra blanket associated with the Timanfaya eruption was emplaced between September 1730 and January 1731, consistent with historical records and the preliminary analysis of Criado et al. (2013). In other words, substantial explosive activity was largely restricted to the initial stages (Phase 1) of the eruption, involving only basanite to alkali basalt magma. Isopleth data indicate eruption column heights reaching at least 8 km during this initial activity. We note that Sharma et al. (2024) arrived at similar column height values based on estimated mass discharge rates for Phase 1 lavas and the model of Mastin et al. (2009). We envisage a pulsating explosive behavior similar to the most explosive phases of the 2021 Cumbre Vieja eruption, which produced ash-rich plumes that were most frequently in the 2–4 km height range but reached up to 8.5 km (Bonadonna et al., 2022). Such activity may be best classified as violent Strombolian (Di Roberto et al., 2016; Taddeucci et al., 2023; Valentine & Gregg, 2008). However, while its duration was similar to the 2021 eruption (~5 vs. 3 months), Phase 1 of the Timanfaya eruption produced a tephra blanket ~20 times as voluminous as Cumbre Vieja's (0.44 km^3 vs. 0.017–0.025 km^3, Bonadonna et al., 2022) and thus it must have been significantly more intense. In contrast, the scarcity of distal tephra layers derived from Phases 2–5 suggest that Phase 1 explosive activity was followed by a durable transition to eruptive styles dominated by lava effusion and mild cone-building Strombolian activity.

To put our findings in a wider context, further comparison of the Timanfaya eruption with other explosive basaltic eruptions is useful. First, we note that the tephra volume produced by the Timanfaya eruption (0.51–0.54 km^3) approaches that of the Laki eruption (0.76 km^3), despite a much smaller total eruptive volume. The tephra blanket at Timanfaya represents 10–16% of the bulk eruption volume — this ratio is lower at Laki (~5%, Thordarson & Self, 1993) but similar at Cumbre Vieja (7–16%, Bonadonna et al., 2022). In Figure 5, the Timanfaya deposits plot above the 2021 Cumbre Vieja deposits (Bonadonna et al., 2022), but below the long-lasting monogenetic events at El Jorullo (1759–1774) and Parícutin (1943–1952), Mexico (Pioli et al., 2008; Rowland et al., 2009), and large basaltic Plinian eruptions, such as the 1886 Tarawera

eruption (Walker et al., 1984), the 122 B.C. Etna eruption (Coltelli et al., 1998) and the late-Pleistocene Fontana Lapilli from the Masaya-Las Sierras volcanic system in Nicaragua (e.g., Costantini et al., 2009).

In terms of plume height, our estimate for Timanfaya compares well with the lower end of values inferred for Laki (6–13 km, Thordarson & Self, 1993) and other explosive basaltic eruptions, such as the 1992 eruption of Cerro Negro (Connor & Connor, 2006). It also coincides, as previously mentioned, with the highest eruption column heights observed for the 2021 eruption at Cumbre Vieja (Bonadonna et al., 2022). Plume height at Timanfaya was however significantly lower than those of the aforementioned basaltic Plinian eruptions, with column heights in the 24–32 km range (Coltelli et al., 1998; Costantini et al., 2009; Walker et al., 1984).

To sum up, our results at Timanfaya, together with the work of Di Roberto et al. (2016) on the 1909 Chinyero eruption on Tenerife and recent direct observations at Cumbre Vieja (Bonadonna et al., 2022; Taddeucci et al., 2023), demonstrate the explosive potential of violent Strombolian activity at Canary Island volcanoes. More broadly, these findings add to a body of evidence documenting significant explosive activity during some cinder cone-producing basaltic eruptions (e.g., Alfano et al., 2019; Bonadonna et al., 2022; Martí et al., 2017; Pioli et al., 2008).

Constraints on volatile emissions

Mounting evidence indicates that Canary Island magmas, as well as similar mafic alkaline magmas from, for instance, the Cape Verde, are volatile-rich and may contain up to several wt.% CO_2, 3 wt.% H_2O and 5,000 ppm S prior to degassing (Burton et al., 2023; DeVitre et al., 2023; Forte et al., 2024; Longpré et al., 2017; Taracsák et al., 2019). Thus, it is expected that an eruption the size of Timanfaya would have released copious amounts of volatiles to the atmosphere. Sharma et al. (2024) measured up to 0.5 wt.% H_2O, 2,650 ppm S, and 1,980 ppm Cl in Timanfaya melt inclusions, but argued that most inclusions represent partially degassed compositions reflecting late-stage entrapment. Based on correlations between S/K_2O and P_2O_5/TiO_2 for inclusions with the highest S concentrations, these authors thus reconstructed undegassed S contents of Timanfaya magmas and obtained a minimum of 1,950 ppm for Calderas Quemadas (Phase 3) and a maximum 3,280 ppm for Caldera de los Cuervos (Phase 1). Using these S concentrations and estimates of lava volume for each eruptive phase, Sharma et al. (2024) applied the “petrologic method” (Devine et al., 1984) to calculate S emissions during the Timanfaya eruption, which yielded a total of 42 ± 10 Tg of SO_2 (21 ± 5 Tg S), with 60% of this figure inferred to have come from Phase 1.

Our trace element data may be utilized to obtain first-order estimates of volatile emissions at Timanfaya, complementary to those obtained from melt inclusion data. Indeed, rare undegassed samples (e.g., Hauri et al., 2018; Le Voyer et al., 2017; Saal et al., 2002) and experimental data (e.g., Rosenthal et al., 2015) indicate that certain trace elements behave similarly to specific volatiles during magmatic processes, with the key difference that they are unaffected by degassing, and therefore can be used to reconstruct undegassed volatile contents (e.g., Anderson & Poland, 2017; Longpré et al., 2017; Michael & Graham, 2015). For instance, Ba and Nb are thought to be good proxies for CO_2 (Michael & Graham, 2015; Rosenthal et al., 2015), whereas Ce, Dy, and K are commonly used for H_2O, S, and Cl, respectively (Koleszar et al., 2009; Michael, 1995; Saal et al., 2002). In Figure 9, we show plots of Cl vs. K_2O, Ba vs. Nb, and Ce vs. Dy for Timanfaya samples, along with corresponding

undegassed volatile element concentrations assuming mantle volatile/lithophile elemental ratios of 105 ± 9 for CO_2/Ba (Michael & Graham, 2015), 505 ± 168 for CO_2/Nb (Rosenthal et al., 2015), 200 ± 50 for H_2O/Ce (Michael, 1995; Saal et al., 2002), 370 +124/-101 for S/Dy (McDonough & Sun, 1995) and 0.11 +0.08/-0.05 for Cl/K (Palme & O'Neill, 2003). While such volatile/lithophile elemental ratios are expected to vary somewhat due to mantle heterogeneity (e.g., Le Voyer et al., 2017), the above values are thought to be reasonable approximations for the Canary Island mantle source, although a S/Dy of 370 is considered conservative as observed values in melt inclusions commonly exceed it, reaching up to 840 (Longpré et al., 2017; Taracsák et al., 2019). Overall, our analysis is consistent with generally high volatile contents (1.5–5 wt.% CO_2, 0.8–3 wt.% H_2O, 1,800–3,000 ppm S, 700–1,800 ppm Cl) in undegassed Timanfaya magmas, with the highest values predicted for the Caldera de los Cuervos basanite (>3.8 wt.% CO_2, >2.3 wt.% H_2O, >2,300 ppm S, ~1,800 ppm Cl). These predicted concentrations broadly agree with the data of Sharma et al. (2024) for S and Cl, but exceed their few measured values for H_2O.

With these reconstructed volatile content ranges in hand, we may in turn apply the petrologic method to calculate rough volatile emissions. We use a conservative eruptive volume of 1.9–3.1 km^3 DRE, obtained by converting a bulk lava volume of 2.2–3.7 km^3 (Longpré and Felpeto, 2021) to 1.7–2.8 km^3 DRE (using our mean lava density of 2,120 kg/m^3 and a magma density of 2,800 kg/m^3) and adding 0.23–0.28 km^3 DRE for tephra (see Tephra volume section). Our calculations also consider a magma crystallinity of 10–20% (Sharma et al., 2024). Assuming 100% syn-eruptive degassing for CO_2 and S [consistent with negligible CO_2 solubility at low pressure (cf. Longpré et al., 2017) and low S concentrations in matrix glasses (Table S4) (Sharma et al., 2024)], initial concentrations of 1.5–5 wt.% CO_2 and 2,000–3,000 ppm S (Fig. 9b,c) yield emissions of 65–388 Tg CO_2 and 9–23 Tg S to the atmosphere, when scaled to the total mass of erupted magma. For chlorine, however, syn-eruptive degassing was incomplete, as attested by significant Cl concentrations remaining in matrix glasses (Fig. 9a). Thus, to estimate Cl emissions, we take the difference between predicted Cl concentrations, obtained based on observed K_2O contents and a Cl/K ratio of 0.11, and matrix glass values, at minimum (Montaña Colorada) and maximum K_2O (Caldera de los Cuervos) contents. This suggests syn-eruptive degassing of 500–1150 ppm Cl, translating to emissions of 2–9 Tg Cl.

Our sulfur emission range overlaps with that of Sharma et al. (2024), but is shifted to lower minimum values. As both studies infer similar undegassed sulfur contents (despite distinct reconstruction methods), this difference likely stems from eruptive mass considerations, which in turn depend on eruptive volume. Indeed, Sharma et al. (2024) listed eruptive volume estimates, broken down into contributions from each eruptive phase, that add up to 5.2 km^3 (bulk), which is higher than the values we used, as outlined above. These estimates, apparently derived from sketches of the lava flow field development (Carracedo et al., 1992), are approximate, however. While our estimates are conservative (mostly due to the unknown, but likely significant amount of lava and tephra that entered the sea), they are constrained by an accurate subaerial lava flow field area, a plausible range of mean lava thicknesses, and field data for tephra presented herein (see also Longpré & Felpeto, 2021). The acquisition of bathymetric (e.g., Soule et al., 2019) and near-surface geophysical (e.g., ground penetrating radar, Gómez-Ortiz et al., 2014) data may help refine the volume — and thus the volatile emissions — of the Timanfaya eruption in the future.

An environmental impact for the Timanfaya eruption?

Overall, the data of Sharma et al. (2024) and the above analysis indicate that volatile emissions at Timanfaya were sizable. For context, Timanfaya's sulfur emissions represent about one third of Laki's, whereas the halogen yields of both eruptions may have been similar (as suggested by the chlorine data). However, while the adverse local and regional effects of Laki's volatile emissions are well documented (Thordarson & Self, 2003), little is known on possible environmental consequences of the Timanfaya eruption, and we briefly review the available data in this section. As discussed by Sharma et al. (2024), ice core evidence for a stratospheric transport of sulfur associated with Timanfaya is ambiguous at best. This is illustrated in Figure 10a, in which only a modest 1731 sulfate anomaly from the GISP2 ice core (Zielinski, 1995) could potentially originate from Timanfaya — more recent multi-core compilations documented Northern Hemisphere anomalies for 1729 (Gao et al., 2008; Sigl et al., 2015) and 1739 (Sigl et al., 2015), but none in the 1730–1736 range. Intriguingly, an analysis of the Global Volcanism Program eruption catalogue yields no obvious candidate for the 1729 sulfate anomaly. In contrast, the 1739 signal is likely tied to the 1739 VEI 5 eruption of Shikotsu (Tarumai) volcano in Japan (Toohey & Sigl, 2017). In any case, the lack of convincing Timanfaya signal in Greenland ice cores is consistent with the tropospheric eruption columns indicated by our data. Based on expected tropospheric circulation patterns over the Canary Islands, the eruption plume might have drifted towards North Africa and the Mediterranean Basin and never have reached Greenland in appreciable quantities (Sharma et al., 2024).

Yet, some climate proxy records hint at a possible environmental impact of the eruption. For instance, a continental-scale temperature reconstruction for Europe and the Arctic (Fig. 10b) (PAGES 2k Consortium, 2013) shows a marked negative anomaly in the first half of the 1730's, but a clear signal for Laki, which might be expected in this record, is lacking. Moreover, the Northern Hemisphere tree ring density network of Briffa et al. (1998) indicates a summer temperature anomaly of –0.25 ˚C for 1731, comparable to –0.27 ˚C for 1783 (Laki) and –0.30 ˚C for 1992 (Pinatubo), and bristlecone pines from the western USA also show a frost ring for 1732 (Salzer & Hughes, 2007). In comparison, however, the Northern Hemisphere composite (N-Tree) of Sigl et al. (2015) displays little to no anomaly contemporaneous with Timanfaya (Fig. 10b). Perhaps most compelling is a multi-proxy reconstruction of annual sea surface temperatures for the tropics (Fig. 10c) (D'Arrigo et al., 2009), which yields an anomaly of –0.90 ˚C for 1731, the coldest value of the past four centuries. In this dataset, 1730 also ranks 12th (–0.69 ˚C), whereas cooling associated with Laki appears minor in the tropics (–0.30 ˚C), consistent with its northern latitude. Finally, environmental effects of the Timanfaya eruption may also be recorded by iron anomalies found in tree rings from the Pyrenees (Hevia et al., 2018) and in historical accounts of dry fog occurrence in Italy (Camuffo & Enzi, 1995). While these integrated observations entertain possible hemispheric environmental repercussions of the Timanfaya eruption — perhaps most acute in the tropics —, they remain somewhat inconclusive. Interestingly, as a side note, the above analysis indicates a marked climate impact for the 1739 Tarumai eruption (Fig. 10a,b).

CONCLUSIONS

The main findings of our investigation of tephra deposits sourced from the 1730–1736 CE Timanfaya eruption may be summarized as follows:

(1) Stratigraphic sections show that explosive activity at Timanfaya was pulsatory and produced a tephra blanket dispersed across most of Lanzarote, but thickest south of the lava flow field, in the area of La Geria. The minimum bulk volume of the tephra blanket is ~0.44 km^3 (0.20 km^3 DRE), representing 10–16% of the total eruption volume (6–10% of total DRE volume). The total tephra volume, including the cones, is 0.51–0.54 km^3 (0.23–0.28 km^3 DRE).

(2) Isopleth data from a particularly thick and coarse basal bed tied to the initial eruptive episode (Caldera de los Cuervos) indicate that the highest eruption columns rose to at least 8 km.

(3) Nearly all distal tephras show basanite–alkali basalt compositions highly enriched in incompatible trace elements that only match tephra originating from the first three vents: Caldera de los Cuervos, Pico Partido and Caldera de Santa Catalina. Distal tephra–source vent correlations confirm these associations and are broadly consistent with the established eruption timeline. Minor discordances between stratigraphy and the eruption timeline may indicate hitherto unrecognized compositional zoning within individual eruptive episodes and/or underappreciated complexities in the eruptive sequence.

(4) Importantly, in line with historical records, our findings confirm that the most explosive activity — probably of violent Strombolian style — was restricted to the initial phase of the eruption, but particularly its first few weeks. Eruption style subsequently transitioned to prolonged, dominantly effusive activity, with minor cone-building Strombolian activity. These results add to a growing body of evidence that mafic Canary Island volcanism, and basaltic fissure eruptions in general, frequently involve vigorous explosive activity.

(5) Our trace element data may be used as coarse proxies for volatiles, indicating that Timanfaya magmas, particularly the early-erupted basanites, were likely volatile-rich (1.5–5 wt.% CO_2, 0.8–3 wt.% H_2O, 1,800–3,000 ppm S, 700–1,800 ppm Cl), consistent with available melt inclusion data. We estimate that the eruption released 65–388 Tg CO_2, 9–23 Tg S, and 2–9 Tg Cl to the atmosphere. For sulfur, our estimate overlaps that of Sharma et al. (2024), with differences mostly due to eruption volume considerations.

(6) The lack of clear sulfate anomaly in Greenland ice cores that could be associated with Timanfaya is consistent with tropospheric eruption column heights and expected atmospheric circulation patterns. However, some climate proxy records may bear a Timanfaya signal, hinting at possible regional/hemispheric environmental repercussions of the eruption.

Future work on the tephra blanket at Timanfaya may be able to resolve the eruption timeline and eruptive dynamics (e.g., fluctuations in eruption column heights) in more detail. In addition, offshore sediment cores may help refine the dispersal and volume of tephra, whereas more robust determination of lava volume may be obtained by near-surface geophysical surveys onland and high-resolution mapping of the submarine extent of the flow field along large portions of the coastline. Additional measurements of volatiles, particularly CO_2 and H_2O, in melt inclusions (and bubbles therein) will allow testing the high undegassed concentrations and fluxes we infer from trace element proxies. Finally, a closer look at climate and environmental

proxy records, especially from North Africa and the Mediterranean Basin, might elucidate whether the Timanfaya eruption had a significant environmental impact beyond Lanzarote.

ACKNOWLEDGEMENTS

This work results from the master's thesis research of J.K.M. at Queens College, City University of New York. We are grateful to the Cabildo de Lanzarote for providing permits to conduct fieldwork and sampling within the Parque Nacional de Timanfaya and the Parque de los Volcanes. We thank Patrick Beaudry, Elena Mateo and Ana Garmendia who helped with fieldwork and Alia Lesnek who helped generating the DEM basemap. Lang Shi and Louise Bolge provided invaluable support during EPMA and LA-ICP-MS analysis, respectively. This work benefitted from discussions with Don Swanson, Ray Cas, Gert-Jan Peeters, William Moreland, Tim Clements, Stephen Self, and Stephen Blake. Jeffrey Marsh and Philipp Ruprecht provided useful comments on an earlier version of this manuscript. We thank two anonymous reviewers and Editor Hannah Dietterich for constructive comments and efficient handling of our manuscript. This work was supported through a Graduate Student Research Grant #11085-15 from the Geological Society of America to J.K.M. and through National Science Foundation Award # 1944723 and a Queens College Research Foundation grant, including partial support from the Paula and Jeffrey Gural Endowed Professorship in Geology, to M.-A.L.

REFERENCES

Alfano, F., Ort, M. H., Pioli, L., Self, S., Hanson, S. L., Roggensack, K., Allison, C. M., Amos, R., & Clarke, A. B. (2019). Subplinian monogenetic basaltic eruption of Sunset Crater, Arizona, USA. *GSA Bulletin*, *131*(3–4), 661–674. https://doi.org/10.1130/B31905.1

Anderson, K. R., & Poland, M. P. (2017). Abundant carbon in the mantle beneath Hawai ‘i. *Nature Geoscience*, 10(9), 704-708. https://doi.org/10.1038/ngeo3007

Aparicio, A., Bustillo, M. A., Garcia, R., & Araña, V. (2006). Metasedimentary xenoliths in the lavas of the Timanfaya eruption (1730–1736, Lanzarote, Canary Islands): Metamorphism and contamination processes. *Geological Magazine*, *143*(2), 181–193. https://doi.org/10.1017/S0016756806001713

Biass, S., Bagheri, G., & Bonadonna, C. (2015). A Matlab implementation of the Carey and Sparks (1986) model to estimate plume height and wind speed from isopleth maps. *Department of Earth Sciences, University of Geneva, Switzerland*. https://vhub.org/resources/3922

Bonadonna, C., & Costa, A. (2012). Estimating the volume of tephra deposits: A new simple strategy. *Geology*, *40*(5), 415–418. https://doi.org/10.1130/G32769.1

Bonadonna, C., Pistolesi, M., Biass, S., Voloschina, M., Romero, J., Coppola, D., Folch, A., D’Auria, L., Martin-Lorenzo, A., & Dominguez, L. (2022). Physical characterization of long-lasting hybrid eruptions: The 2021 Tajogaite eruption of Cumbre Vieja (La Palma, Canary Islands). *Journal of Geophysical Research: Solid Earth*, *127*(11), e2022JB025302. https://doi.org/10.1029/2022JB025302

Briffa, K. R., Jones, P. D., Schweingruber, F. H., & Osborn, T. J. (1998). Influence of volcanic eruptions on Northern Hemisphere summer temperature over the past 600 years. *Nature*, *393*(6684), 450–455. https://doi.org/10.1038/30943

Brown, R. J., Blake, S., Thordarson, T., & Self, S. (2014). Pyroclastic edifices record vigorous lava fountains during the emplacement of a flood basalt flow field, Roza Member, Columbia River Basalt Province, USA. *GSA Bulletin*, *126*(7–8), 875–891. https://doi.org/10.1130/B30857.1

Brown, R. J., Thordarson, T., Self, S., & Blake, S. (2015). Disruption of tephra fall deposits caused by lava flows during basaltic eruptions. *Bulletin of Volcanology*, *77*, 1–15. https://doi.org/10.1007/s00445-015-0974-3

Burton, M., Aiuppa, A., Allard, P., Asensio-Ramos, M., Cofrades, A. P., La Spina, A., Nicholson, E. J., Zanon, V., Barrancos, J., & Bitetto, M. (2023). Exceptional eruptive CO_2 emissions from intra-plate alkaline magmatism in the Canary volcanic archipelago. *Communications Earth & Environment*, 4(1), 467. https://doi.org/10.1038/s43247-023-01103-x

Camuffo, D., & Enzi, S. (1995). Impact of the clouds of volcanic aerosols in Italy during the last 7 centuries. *Natural Hazards*, *11*, 135–161. https://doi.org/10.1007/BF00634530

Carey, S., & Sparks, R. S. J. (1986). Quantitative models of the fallout and dispersal of tephra from volcanic eruption columns. *Bulletin of Volcanology*, *48*, 109–125. https://doi.org/10.1007/BF01046546

Carracedo, J. (2014). The 1730–1736 Eruption of Lanzarote, Canary Islands. In F. Gutiérrez & M. Gutiérrez (Eds.), *Landscapes and Landforms of Spain* (pp. 273–288). Springer Netherlands. https://doi.org/10.1007/978-94-017-8628-7_23

Carracedo, J. C., & Rodríguez Badiola, E. (1991). *Lanzarote. La erupción volcánica de 1730*. Cabildo Insular de Lanzarote, Servicios de Publicaciones.

Carracedo, J. C., Rodríguez Badiola, E., & Soler, V. (1990). Aspectos volcanológicos y estructurales, evolución petrológica e implicaciones en riesgo volcánico de la erupción de 1730 en Lanzarote, Islas Canarias. *Estudios Geológicos*, *46*(1–2), 25–55. https://doi.org/10.3989/egeol.90461-2436

Carracedo, J. C., Rodríguez Badiola, E., & Soler, V. (1992). The 1730-1736 eruption of Lanzarote, Canary Islands: A long, high-magnitude basaltic fissure eruption. *Journal of Volcanology and Geothermal Research*, *53*(1–4), 239–250. https://doi.org/10.1016/0377-0273(92)90084-Q

Carracedo, J. C., Singer, B., Jicha, B., Guillou, H., Rodríguez Badiola, E., Meco, J., Pérez Torrado, F. J., Gimeno, D., Socorro, J. S., & Láinez, A. (2003). La erupción y el tubo volcánico del Volcán Corona (Lanzarote, Islas Canarias). *Estudios Geológicos*, *59*(5–6), 277–302. http://hdl.handle.net/10261/2329

Carracedo, J. C., Troll, V. R., Day, J. M., Geiger, H., Aulinas, M., Soler, V., Deegan, F. M., Perez-Torrado, F. J., Gisbert, G., & Gazel, E. (2022). The 2021 eruption of the Cumbre Vieja volcanic ridge on La Palma, Canary Islands. *Geology Today*, *38*(3), 94–107. https://doi.org/10.1111/gto.12388

Coello, J., Cantagrel, J. M., Hernan, F., Fuster, J. M., Ibarrola, E., Ancochea, E., Casquet, C., Jamond, C., Diaz De Teran, J. R., & Cendrero, A. (1992). Evolution of the eastern volcanic ridge of the Canary Islands based on new K-Ar data. *Journal of Volcanology and Geothermal Research*, *53*(1–4), 251–274. https://doi.org/10.1016/0377-0273(92)90085-R

Coltelli, M., Del Carlo, P., & Vezzoli, L. (1998). Discovery of a Plinian basaltic eruption of Roman age at Etna volcano, Italy. *Geology*, *26*(12), 1095–1098. https://doi.org/10.1130/0091-7613(1998)026<1095:DOAPBE>2.3.CO;2

Connor, L. J., & Connor, C. B. (2006). Inversion is the key to dispersion: Understanding eruption dynamics by inverting tephra fallout. In H. M. Mader, S. G. Coles, C. B. Connor, & L. J. Connor (Eds.), *Statistics in Volcanology* (Vol. 1, p. 0). Geological Society of London. https://doi.org/10.1144/IAVCEI001.18

Costantini, L., Bonadonna, C., Houghton, B., & Wehrmann, H. (2009). New physical characterization of the Fontana Lapilli basaltic Plinian eruption, Nicaragua. *Bulletin of Volcanology*, *71*(3), 337–355. https://doi.org/10.1007/s00445-008-0227-9

Criado, C., Dorta, P., Bethencourt, J., Navarro, J., Romero, C., & García, C. (2013). Evidence of historic infilling of valleys in Lanzarote after the Timanfaya eruption (AD 1730–1736, Canary Islands, Spain). *The Holocene*, *23*(12), 1786–1796. https://doi.org/10.1177/0959683613505342

Daggitt, M. L., Mather, T. A., Pyle, D. M., & Page, S. (2014). AshCalc–a new tool for the comparison of the exponential, power-law and Weibull models of tephra deposition. *Journal of Applied Volcanology*, *3*, 1–8. https://doi.org/10.1186/2191-5040-3-7

D'Arrigo, R., Wilson, R., & Tudhope, A. (2009). The impact of volcanic forcing on tropical temperatures during the past four centuries. *Nature Geoscience*, *2*(1), 51–56. https://doi.org/10.1038/ngeo393

Devine, J. D., Gardner, J. E., Brack, H. P., Layne, G. D., & Rutherford, M. J. (1995). Comparison of microanalytical methods for estimating H2O contents of silicic volcanic glasses. *American Mineralogist*, *80*(3–4), 319–328. https://doi.org/10.2138/am-1995-3-413

Devine, J. D., Sigurdsson, H., Davis, A. N., & Self, S. (1984). Estimates of sulfur and chlorine yield to the atmosphere from volcanic eruptions and potential climatic effects. *Journal of Geophysical Research*, *89*(B7), 6309–6325. https://doi.org/10.1029/JB089iB07p06309

DeVitre, C. L., Gazel, E., Ramalho, R. S., Venugopal, S., Steele-MacInnis, M., Hua, J., Allison, C. M., Moore, L. R., Carracedo, J. C., & Monteleone, B. (2023). Oceanic intraplate explosive eruptions fed directly from the mantle. *Proceedings of the National Academy of Sciences*, 120(33), e2302093120. https://doi.org/10.1073/pnas.2302093120

Di Roberto, A., Bertagnini, A., Del Carlo, P., Meletlidis, S., & Pompilio, M. (2016). The 1909 Chinyero eruption on Tenerife (Canary Islands): Insights from historical accounts, and tephrostratigraphic and geochemical data. Bulletin of Volcanology, 78(12), 88. https://doi.org/10.1007/s00445-016-1083-7

Engwell, S. L., Aspinall, W. P., & Sparks, R. S. J. (2015). An objective method for the production of isopach maps and implications for the estimation of tephra deposit volumes and their uncertainties. *Bulletin of Volcanology*, *77*(61), 1–18. https://doi.org/10.1007/s00445-015-0942-y

Forte, F. M. L., Schiavi, F., Rose-Koga, E. F., Rotolo, S. G., Verdier-Paoletti, M., Aiuppa, A., & Zanon, V. (2024). High CO_2 in the mantle source of ocean island basanites. *Geochimica et Cosmochimica Acta*. https://doi.org/10.1016/j.gca.2024.01.016

Gao, C., Robock, A., & Ammann, C. (2008). Volcanic forcing of climate over the past 1500 years: An improved ice core-based index for climate models. *Journal of Geophysical Research*, *113*(D23), D23111. https://doi.org/10.1029/2008jd010239

Glaze, L. S., Self, S., Schmidt, A., & Hunter, S. J. (2017). Assessing eruption column height in ancient flood basalt eruptions. *Earth and Planetary Science Letters*, *457*, 263–270. https://doi.org/10.1016/j.epsl.2014.07.043

Gómez-Ortiz, D., Montesinos, F. G., Martín-Crespo, T., Solla, M., Arnoso, J., & Vélez, E. (2014). Combination of geophysical prospecting techniques into areas of high protection value: Identification of shallow volcanic structures. *Journal of Applied Geophysics*, *109*, 15–26. https://doi.org/10.1016/j.jappgeo.2014.07.009

Gómez-Ulla, A., Sigmarsson, O., & Gudfinnsson, G. H. (2017). Trace element systematics of olivine from historical eruptions of Lanzarote, Canary Islands: Constraints on mantle source and melting mode. *Chemical Geology*, *449*, 99–111. https://doi.org/10.1016/j.chemgeo.2016.11.021

Gómez-Ulla, A., Sigmarsson, O., Huertas, M. J., Devidal, J.-L., & Ancochea, E. (2018). The historical basanite-alkali basalt-tholeiite suite at Lanzarote, Canary Islands: Carbonated melts of heterogeneous mantle source? *Chemical Geology*, *494*, 56–68. https://doi.org/10.1016/j.chemgeo.2018.07.015

Gudmundsson, M. T., Jónsdóttir, K., Hooper, A., Holohan, E. P., Halldórsson, S. A., Ófeigsson, B. G., Cesca, S., Vogfjörd, K. S., Sigmundsson, F., Högnadóttir, T., Einarsson, P., Sigmarsson, O., Jarosch, A. H., Jónasson, K., Magnússon, E., Hreinsdóttir, S., Bagnardi, M., Parks, M. M., Hjörleifsdóttir, V., … Aiuppa, A. (2016). Gradual caldera collapse at Bárdarbunga volcano, Iceland, regulated by lateral magma outflow. *Science*, *353*(6296), 262. https://doi.org/10.1126/science.aaf8988

Hartley, M. E., Maclennan, J., Edmonds, M., & Thordarson, T. (2014). Reconstructing the deep CO_2 degassing behaviour of large basaltic fissure eruptions. *Earth and Planetary Science Letters*, *393*, 120–131. https://doi.org/10.1016/j.epsl.2014.02.031

Hauri, E. H., Maclennan, J., McKenzie, D., Gronvold, K., Oskarsson, N., & Shimizu, N. (2018). CO_2 content beneath northern Iceland and the variability of mantle carbon. *Geology*, 46(1), 55-58. https://doi.org/10.1130/G39413.1

Hevia, A., Sánchez-Salguero, R., Camarero, J. J., Buras, A., Sangüesa-Barreda, G., Galván, J. D., & Gutiérrez, E. (2018). Towards a better understanding of long-term wood-chemistry variations in old-growth forests: A case study on ancient Pinus uncinata trees from the Pyrenees. *Science of the Total Environment*, *625*, 220–232. https://doi.org/10.1016/j.scitotenv.2017.12.229

Hill, B. E., Connor, C. B., Jarzemba, M. S., La Femina, P. C., Navarro, M., & Strauch, W. (1998). 1995 eruptions of Cerro Negro Volcano, Nicaragua, and risk assessment for future eruptions. *GSA Bulletin*, *110*(10), 1231–1241. https://doi.org/10.1130/0016-7606(1998)110<1231:EOCNVN>2.3.CO;2

Houghton, B. F., & Wilson, C. J. N. (1989). A vesicularity index for pyroclastic deposits. *Bulletin of Volcanology*, *51*, 451–462. https://doi.org/10.1007/BF01078811

Jahn, R., & Stahr, K. (1996). Development of soils and site qualities on basic volcanoclastics with special reference to the semiarid environment of Lanzarote, Canary Islands, Spain. *Revista Mexicana de Ciencias Geológicas*, *13*(1), 104–112.

Jarosewich, E. (2002). Smithsonian microbeam standards. *Journal of Research of the National Institute of Standards and Technology*, *107*(6), 681–685. https://doi.org/10.6028/jres.107.054

Jochum, K. P., & Nohl, U. (2008). Reference materials in geochemistry and environmental research and the GeoReM database. *Chemical Geology*, *253*(1), 50–53. https://doi.org/10.1016/j.chemgeo.2008.04.002

Johnson, D., Hooper, P., & Conrey, R. (1999). XRF analysis of rocks and minerals for major and trace elements on a single low dilution Li-tetraborate fused bead. *Advances in X-Ray Analysis*, *41*, 843–867.

Kervyn, M., Ernst, G. G. J., Carracedo, J. C., & Jacobs, P. (2012). Geomorphometric variability of "monogenetic" volcanic cones: Evidence from Mauna Kea, Lanzarote and experimental cones. *Geomorphology*, *136*(1), 59–75. https://doi.org/10.1016/j.geomorph.2011.04.009

Knaack, C., Cornelius, S., & Hooper, P. R. (1994). Trace element analyses of rocks and minerals by ICP-MS. *Open File Report, Department of Geology, Washington State University*.

Koleszar, A. M., Saal, A. E., Hauri, E. H., Nagle, A. N., Liang, Y., & Kurz, M. D. (2009). The volatile contents of the Galapagos plume; evidence for H_2O and F open system behavior in melt inclusions. *Earth and Planetary Science Letters*, 287(3-4), 442-452. https://doi.org/10.1016/j.epsl.2009.08.029

Kueppers, U., Scheu, B., Spieler, O., & Dingwell, D. B. (2005). Field-based density measurements as tool to identify preeruption dome structure: Set-up and first results from Unzen volcano, Japan. *Journal of Volcanology and Geothermal Research*, *141*(1–2), 65–75. https://doi.org/10.1016/j.jvolgeores.2004.09.005

Le Bas, M. J., Le Maitre, R. W., Streckeisen, A., & Zanettin, B. (1986). A chemical classification of volcanic rocks based on the total alkali-silica diagram. *Journal of Petrology*, *27*(3), 745–750. https://doi.org/10.1093/petrology/27.3.745

Le Voyer, M., Kelley, K. A., Cottrell, E., & Hauri, E. H. (2017). Heterogeneity in mantle carbon content from CO_2-undersaturated basalts. *Nature Communications*, 8, 14062. https://doi.org/10.1038/ncomms14062

Longpré, M.-A., & Felpeto, A. (2021). Historical volcanism in the Canary Islands; part 1: A review of precursory and eruptive activity, eruption parameter estimates, and implications for hazard assessment. *Journal of Volcanology and Geothermal Research*, *419*, 107363. https://doi.org/10.1016/j.jvolgeores.2021.107363

Longpré, M.-A., Stix, J., Costa, F., Espinoza, E., & Muñoz, A. (2014). Magmatic processes and associated timescales leading to the January 1835 eruption of Cosigüina volcano, Nicaragua. *Journal of Petrology*, *55*(6), 1173–1201. https://doi.org/10.1093/petrology/egu022

Longpré, M.-A., Stix, J., Klügel, A., & Shimizu, N. (2017). Mantle to surface degassing of carbon- and sulphur-rich alkaline magma at El Hierro, Canary Islands. *Earth and Planetary Science Letters*, *460*, 268–280. https://doi.org/10.1016/j.epsl.2016.11.043

Lundstrom, C. C., Hoernle, K., & Gill, J. (2003). U-series disequilibria in volcanic rocks from the Canary Islands: Plume versus lithospheric melting. *Geochimica et Cosmochimica Acta*, *67*(21), 4153–4177. https://doi.org/10.1016/s0016-7037(03)00308-9

Martí, J., Planagumà, L. I, Geyer, A., Aguirre-Díaz, G., Pedrazzi, D., & Bolós, X. (2017). Basaltic ignimbrites in monogenetic volcanism: The example of La Garrotxa volcanic field. *Bulletin of Volcanology*, *79*, 1–12. https://doi.org/10.1007/s00445-017-1113-0

Mastin, L. G., Guffanti, M., Servranckx, R., Webley, P., Barsotti, S., Dean, K., ... & Waythomas, C. F. (2009). A multidisciplinary effort to assign realistic source parameters to models of volcanic ash-cloud transport and dispersion during eruptions. *Journal of Volcanology and Geothermal Research*, 186(1-2), 10-21. https://doi.org/10.1016/j.jvolgeores.2009.01.008

McDonough, W. F., & Sun, S. -s. (1995). The composition of the Earth. *Chemical Geology*, *120*(3–4), 223–253. https://doi.org/10.1016/0009-2541(94)00140-4

Michael, P. (1995). Regionally distinctive sources of depleted MORB: evidence from trace elements and H_2O. *Earth and Planetary Science Letters*, *131*(3), 301–320. https://doi.org/10.1016/0012-821X(95)00023-6

Michael, P. J., & Graham, D. W. (2015). The behavior and concentration of CO_2 in the suboceanic mantle: Inferences from undegassed ocean ridge and ocean island basalts. *Lithos*, *236–237*, 338–351. https://doi.org/10.1016/j.lithos.2015.08.020

Neal, C. A., Brantley, S. R., Antolik, L., Babb, J. L., Burgess, M., Calles, K., Cappos, M., Chang, J. C., Conway, S., Desmither, L., Dotray, P., Elias, T., Fukunaga, P., Fuke, S., Johanson, I. A., Kamibayashi, K., Kauahikaua, J., Lee, R. L., Pekalib, S., … Damby, D. (2019). The 2018 rift eruption and summit collapse of Kīlauea Volcano. *Science*, *363*(6425), 367–374. https://doi.org/10.1126/science.aav7046

PAGES 2k Consortium. (2013). Continental-scale temperature variability during the past two millennia. *Nature Geoscience*, *6*(5), 339–346. https://doi.org/10.1038/ngeo1797

Pallarés Padilla, A. (2007). Nuevas aportaciones al conocimiento de la erupción de Timanfaya (Lanzarote). *Académico de Número, Academia de Ciencias e Ingenierías de Lanzarote*, 45.

Palme, H., & O'Neill, H. S. C. (2003). Cosmochemical estimates of mantle composition. *Treatise on Geochemistry*, *2*, 1–38. https://doi.org/10.1016/B0-08-043751-6/02177-0

Perez-Torrado, F. J., Carracedo, J. C., Guillou, H., Rodriguez-Gonzalez, A., & Fernandez-Turiel, J. L. (2023). Age, duration and spatial distribution of ocean shields and rejuvenated volcanism: Fuerteventura and Lanzarote, Eastern Canaries. *Journal of the Geological Society*, *180*(4), jgs2022-112. https://doi.org/10.1144/jgs2022-112

Pioli, L., Erlund, E., Johnson, E., Cashman, K., Wallace, P., Rosi, M., & Delgado Granados, H. (2008). Explosive dynamics of violent Strombolian eruptions: The eruption of Parícutin Volcano 1943–1952 (Mexico). *Earth and Planetary Science Letters*, *271*(1–4), 359–368. https://doi.org/10.1016/j.epsl.2008.04.026

Pyle, D. M. (1989). The thickness, volume and grainsize of tephra fall deposits. *Bulletin of Volcanology*, *51*(1), 1–15. https://doi.org/10.1007/BF01086757

Reiners, P. W. (2002). Temporal-compositional trends in intraplate basalt eruptions: Implications for mantle heterogeneity and melting processes. *Geochemistry, Geophysics, Geosystems*, *3*(2), 1–30. https://doi.org/10.1029/2001GC000250

Robock, A. (2000). Volcanic eruptions and climate. *Reviews of Geophysics*, *38*(2), 191–219. https://doi.org/10.1029/1998rg000054

Romero, C. (2003). *El relieve de Lanzarote*. Servicio de Publicaciones, Cabildo de Lanzarote.

Rosenthal, A., Hauri, E. H., & Hirschmann, M. M. (2015). Experimental determination of C, F, and H partitioning between mantle minerals and carbonated basalt, CO_2/Ba and CO_2/Nb systematics of partial melting, and the CO_2 contents of basaltic source regions. *Earth and Planetary Science Letters*, *412*(0), 77–87. https://doi.org/10.1016/j.epsl.2014.11.044

Rowland, S. K., Jurado-Chichay, Z., Ernst, G., & Walker, G. P. L. (2009). Pyroclastic deposits and lava flows from the 1759–1774 eruption of El Jorullo, México: Aspects of 'violent Strombolian' activity and comparison with Parícutin. In T. Thordarson, S. Self, G. Larsen, S. K. Rowland, & Á. Höskuldsson (Eds.), *Studies in Volcanology: The Legacy of George Walker* (Vol. 2, p. 0). Geological Society of London. https://doi.org/10.1144/IAVCEI002.6

Saal, A. E., Hauri, E. H., Langmuir, C. H., & Perfit, M. R. (2002). Vapour undersaturation in primitive mid-ocean-ridge basalt and the volatile content of Earth's upper mantle. *Nature*, *419*(6906), 451–455. https://doi.org/10.1038/nature01073

Salzer, M. W., & Hughes, M. K. (2007). Bristlecone pine tree rings and volcanic eruptions over the last 5000 yr. *Quaternary Research*, *67*(1), 57–68. https://doi.org/10.1016/j.yqres.2006.07.004

Schmincke, H.-U., Klügel, A., Hansteen, T. H., Hoernle, K., & van den Bogaard, P. (1998). Samples from the Jurassic ocean crust beneath Gran Canaria, La Palma and Lanzarote (Canary Islands). *Earth and Planetary Science Letters*, *163*(1–4), 343–360. https://doi.org/10.1016/S0012-821X(98)00168-X

Self, S., Widdowson, M., Thordarson, T., & Jay, A. E. (2006). Volatile fluxes during flood basalt eruptions and potential effects on the global environment: A Deccan perspective. *Earth and Planetary Science Letters*, *248*(1–2), 518–532. https://doi.org/10.1016/j.epsl.2006.05.041

Sharma, K. (2005). *The eruptions of Öræfajökull 1362 (Iceland) and Lanzarote 1730-36 (Canary Islands): Sulphur emissions and volcanology*. PhD Thesis, The Open University, 293 pp.

Sharma, K., Blake, S., & Self, S. (2024). SO_2 emissions from the Timanfaya eruption (1730–36 CE), Lanzarote, Canary Islands. *Journal of Volcanology and Geothermal Research*, 445, 107984. https://doi.org/10.1016/j.jvolgeores.2023.107984

Sigl, M., Winstrup, M., McConnell, J. R., Welten, K. C., Plunkett, G., Ludlow, F., Buntgen, U., Caffee, M., Chellman, N., Dahl-Jensen, D., Fischer, H., Kipfstuhl, S., Kostick, C., Maselli, O. J., Mekhaldi, F., Mulvaney, R., Muscheler, R., Pasteris, D. R., Pilcher, J. R., … Woodruff, T. E. (2015). Timing and climate forcing of volcanic eruptions for the past 2,500 years. *Nature*, *523*(7562), 543–549. https://doi.org/10.1038/nature14565

Sigmarsson, O., Carn, S., & Carracedo, J. C. (1998). Systematics of U-series nuclides in primitive lavas from the 1730–36 eruption on Lanzarote, Canary Islands, and implications for the role of garnet pyroxenites during oceanic basalt formations. *Earth and Planetary Science Letters*, *162*(1), 137–151. https://doi.org/10.1016/S0012-821X(98)00162-9

Solana, M. C., Kilburn, C. R. J., Rodriguez Badiola, E., & Aparicio, A. (2004). Fast emplacement of extensive pāhoehoe flow-fields: The case of the 1736 flows from Montaña de las Nueces, Lanzarote. *Journal of Volcanology and Geothermal Research*, *132*(2–3), 189–207. https://doi.org/10.1016/S0377-0273(03)00345-7

Soule, A., Heffron, E., Gee, L., Mayer, L., Raineault, N. A., German, C. R., Lim, D., Zoeller, M. H., & Parcheta, C. (2019). Mapping the lava deltas of the 2018 eruption of Kīlauea Volcano. *Oceanography*, *32*(1), 46–47. USGS Publications Warehouse. https://doi.org/10.5670/oceanog.2019.supplement.01

Stix, J., Gauthier, G., & Ludden, J. N. (1995). A critical look at quantitative laser-ablation ICP-MS analysis of natural and synthetic glasses. *The Canadian Mineralogist*, *33*(2), 435–444.

Taddeucci, J., Scarlato, P., Andronico, D., Ricci, T., Civico, R., Del Bello, E., ... & Pérez, N. M. (2023). The explosive activity of the 2021 Tajogaite eruption (La Palma, Canary Islands, Spain). *Geochemistry, Geophysics, Geosystems*, *24*(6), e2023GC010946.

Taracsák, Z., Hartley, M. E., Burgess, R., Edmonds, M., Iddon, F., & Longpré, M.-A. (2019). High fluxes of deep volatiles from ocean island volcanoes: Insights from El Hierro, Canary Islands. *Geochimica et Cosmochimica Acta*, *258*, 19–36. https://doi.org/10.1016/j.gca.2019.05.020

Thomas, L. E., Hawkesworth, C. J., Van Calsteren, P., Turner, S. P., & Rogers, N. W. (1999). Melt generation beneath ocean islands: A U-Th-Ra isotope study from Lanzarote in the Canary Islands. *Geochimica et Cosmochimica Acta*, *63*(23–24), 4081–4099. https://doi.org/10.1016/s0016-7037(99)00310-5

Thordarson, T., & Larsen, G. (2007). Volcanism in Iceland in historical time: Volcano types, eruption styles and eruptive history. *Journal of Geodynamics*, *43*(1), 118–152. https://doi.org/10.1016/j.jog.2006.09.005

Thordarson, T., & Self, S. (1993). The Laki (Skaftár Fires) and Grímsvötn eruptions in 1783–1785. *Bulletin of Volcanology*, *55*(4), 233–263. https://doi.org/10.1007/BF00624353

Thordarson, T., & Self, S. (2003). Atmospheric and environmental effects of the 1783–1784 Laki eruption: A review and reassessment. *Journal of Geophysical Research: Atmospheres*, *108*(D1), 4011. https://doi.org/10.1029/2001JD002042

Thordarson, T., Self, S., Óskarsson, N., & Hulsebosch, T. (1996). Sulfur, chlorine, and fluorine degassing and atmospheric loading by the 1783–1784 AD Laki (Skaftár Fires) eruption in Iceland. *Bulletin of Volcanology*, *58*(2), 205–225. https://doi.org/10.1007/s004450050136

Toohey, M., & Sigl, M. (2017). Volcanic stratospheric sulfur injections and aerosol optical depth from 500 BCE to 1900 CE. *Earth System Science Data*, *9*(2), 809–831. https://doi.org/10.5194/essd-9-809-2017

Troll, V. R., Carracedo, J. C., Jägerup, B., Streng, M., Barker, A. K., Deegan, F. M., Perez-Torrado, F., Rodriguez-Gonzalez, A., & Geiger, H. (2017). Volcanic particles in agriculture and gardening. *Geology Today*, *33*(4), 148–154. https://doi.org/10.1111/gto.12193

Troll, V. R., Klügel, A., Longpré, M.-A., Burchardt, S., Deegan, F. M., Carracedo, J. C., Wiesmaier, S., Kueppers, U., Dahren, B., Blythe, L. S., Hansteen, T. H., Freda, C., Budd, D. A., Jolis, E. M., Jonsson, E., Meade, F. C., Harris, C., Berg, S. E., Mancini, L., … Pedroza, K. (2012). Floating stones off El Hierro, Canary Islands: Xenoliths of pre-island sedimentary origin in the early products of the October 2011 eruption. *Solid Earth*, *3*(1), 97–110. https://doi.org/10.5194/se-3-97-2012

Valentine, G. A., & Gregg, T. K. P. (2008). Continental basaltic volcanoes—Processes and problems. *Journal of Volcanology and Geothermal Research*, *177*(4), 857–873. https://doi.org/10.1016/j.jvolgeores.2008.01.050

van den Bogaard, P. (2013). The origin of the Canary Island Seamount Province-New ages of old seamounts. *Scientific Reports*, *3*, 2107. https://doi.org/10.1038/srep02107

von Suchodoletz, H., Fuchs, M., & Zöller, L. (2008). Dating Saharan dust deposits on Lanzarote (Canary Islands) by luminescence dating techniques and their implication for palaeoclimate reconstruction of NW Africa. *Geochemistry, Geophysics, Geosystems*, *9*(2), Q02Q07. https://doi.org/10.1029/2007GC001658

Walker, G. P. L., Self, S., & Wilson, L. (1984). Tarawera 1886, New Zealand—A basaltic plinian fissure eruption. *Journal of Volcanology and Geothermal Research*, *21*(1–2), 61–78. https://doi.org/10.1016/0377-0273(84)90016-7

White, J. D. L., & Houghton, B. F. (2006). Primary volcaniclastic rocks. *Geology*, *34*(8), 677–680. https://doi.org/10.1130/g22346.1

Zaczek, K., Troll, V. R., Cachao, M., Ferreira, J., Deegan, F. M., Carracedo, J. C., Soler, V., Meade, F. C., & Burchardt, S. (2015). Nannofossils in 2011 El Hierro eruptive products reinstate plume model for Canary Islands. *Scientific Reports*, *5*, 7945. https://doi.org/10.1038/srep07945

Zielinski, G. A. (1995). Stratospheric loading and optical depth estimates of explosive volcanism over the last 2100 years derived from the Greenland Ice Sheet Project 2 ice core. *Journal of Geophysical Research*, *100*(D10), 20937–20955. https://doi.org/10.1029/95jd01751

FIGURES

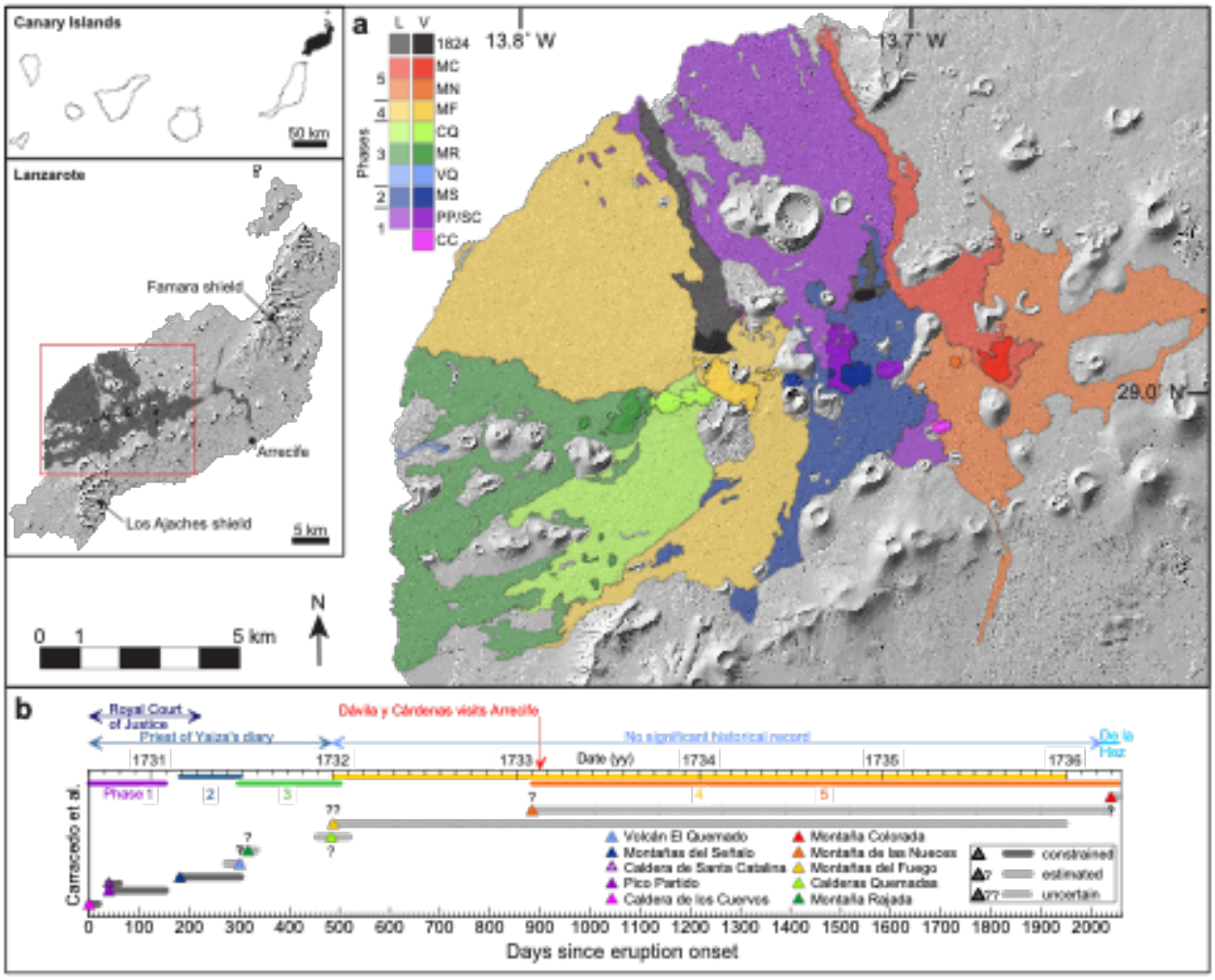

Figure 1. Map of Timanfaya lava flows and eruption timeline. (a) Digital elevation model of Lanzarote showing the 1730–1736 lava flows (L) and the location of associated source vents (V), after Carracedo and Rodríguez Badiola (1991). The color code refers to the eruption timeline in (b), from earliest to latest: (Phase 1) CC: Caldera de los Cuervos; PP/SC: Pico Partido and Caldera de Santa Catalina; (Phase 2) MS: Montañas del Señalo; (Phase 3) VQ: Volcán El Quemado; MR: Montaña Rajada; CQ: Calderas Quemadas; (Phase 4) MF: Montañas del Fuego; (Phase 5) MN: Montaña de las Nueces; MC: Montaña Colorada. First inset: Map of the Canary Islands with Lanzarote shown in black. Second inset: Map of Lanzarote showing the full extent of the 1730–1736 flow field in gray and the area expanded in (a) (red rectangle). (b) Eruption timeline modified after Longpré and Felpeto (2021), based on historical records and geologic mapping (Carracedo et al., 1990, 1992; Carracedo & Rodríguez Badiola, 1991). See text for details.

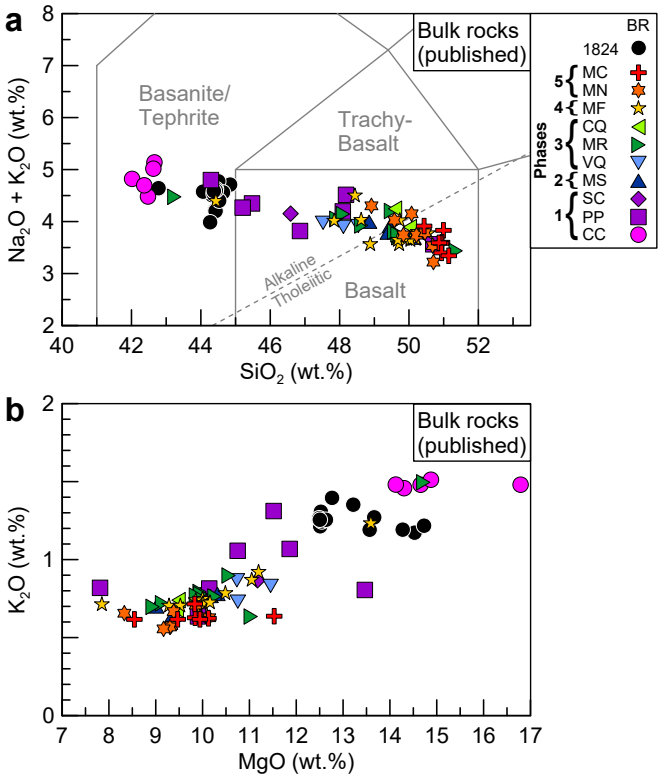

Figure 2. The temporal–compositional trend of Timanfaya lavas and tephras. (a) Total alkalis vs. silica diagram (TAS) (Le Bas et al., 1986) and (b) K_2O vs. MgO contents for published bulk rock (BR) data (Carracedo et al., 1990; Gómez-Ulla et al., 2017; Thomas et al., 1999), defining the early, high-MgO basanite to late tholeiite trend. Sample identification (symbol and color code in key next to panel (a) applies to all panels and subsequent figures): CC: Caldera de los Cuervos; PP: Pico Partido; SC: Caldera de Santa Catalina; MS: Montañas del Señalo; VQ: Volcán El Quemado; MR: Montaña Rajada; CQ: Calderas Quemadas; MF: Montañas del Fuego; MN: Montaña de las Nueces; MC: Montaña Colorada (see Figure 1).

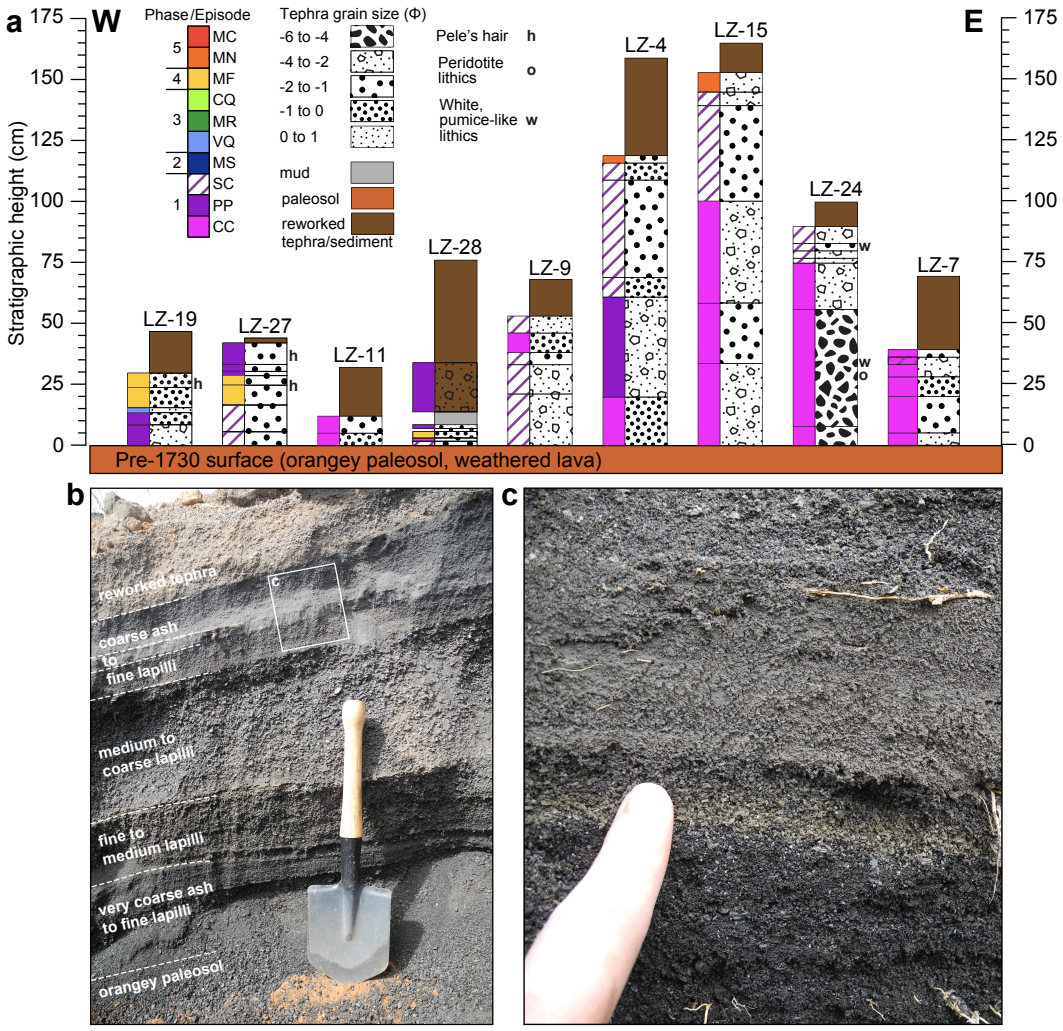

Figure 3. Stratigraphy of Timanfaya tephras. (a) Stratigraphic columns of selected trench localities (see Fig. 4) show grain size, as average clast diameter from each bed. Colored bars on the left-hand side indicate corresponding source vent, as determined by geochemical correlation. All sections along with sample numbers are provided in Fig. S1. (b) Picture of representative section (near site LZ-4), with an orangey paleosol at its base, interbedded lapilli and ash in the middle, and an upper brownish layer interpreted to be reworked. Shovel is 50-cm-long for scale. (c) Close-up on the upper part of the same section (white box in (b)) showing a thin layer of distinctive golden frothy lapilli resembling those found on the flanks Montaña Colorada.

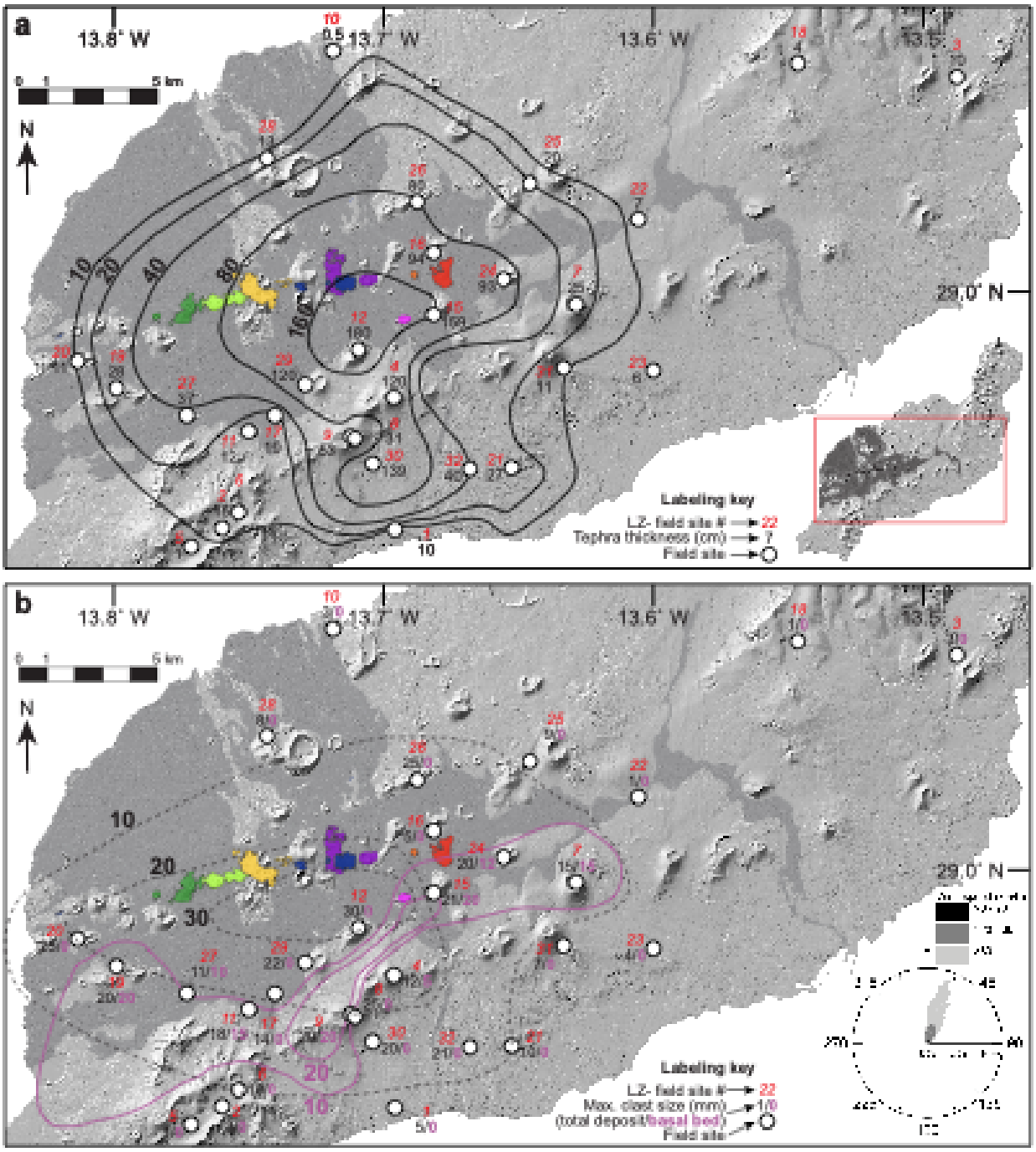

Figure 4. Isopach and isopleth maps. (a) Isopach map showing total tephra deposit thickness, with 10, 20, 40, 80, and 160 cm contours (bold font). Individual field sites are indicated by a white circle, with a two-digit label. The digit in red italic font is the field site number (LZ-number, see also Figs. 3 and S1, Table S1), and the digit in black font is the total tephra thickness in cm. Inset: Map of Lanzarote showing the area expanded in this figure (red rectangle). (b) Map showing two sets of isopleths for maximum clast size (in mm). Isopleths for the total deposit are shown by black dashed lines and bold font, while isopleths for a particularly coarse and thick

basal bed tied to Caldera de los Cuervos based on stratigraphic position and geochemical composition are shown by magenta solid lines and bold font. Site labels record site number (red italic) and maximum clast size (total deposit: black font; basal bed only: magenta bold font). Inset: Rose diagram showing wind directions and speed at 100 m altitude near Arrecife (Fig. 1), in the time period from 2000 to 2020 (data from open-meteo.com). In both (a) and (b), the location of the 1730–1736 lava flow (gray) and main vents are shown for reference (see Fig. 1).

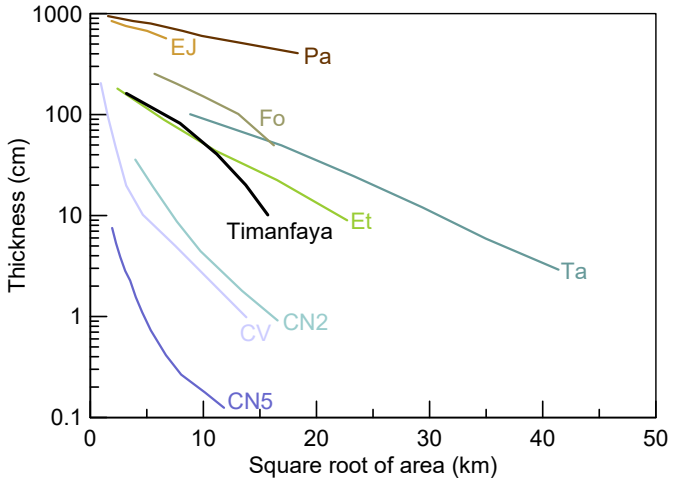

Figure 5. Tephra deposit thickness versus square root of isopach area. The Timanfaya tephra blanket is compared with other basaltic eruptions, including long-lasting cone-forming eruptions [Pa: 1943–1952 Parícutin, (Pioli et al., 2008); EJ: 1759–1774 CE El Jorullo (Rowland et al., 2009); CV: 2021 Cumbre Vieja (Bonadonna et al., 2022)], Plinian eruptions [Fo: 60 ka Fontana Lapilli (Costantini et al., 2009); Ta: 1886 CE Tarawera (Walker et al., 1984); Et: 122 BC Etna (Coltelli et al., 1998)] and two contrasting eruptions of Cerro Negro, Nicaragua [CN2: 1992 VEI 3 (Connor & Connor, 2006); CN5: 1995 VEI 2 (Hill et al., 1998)].

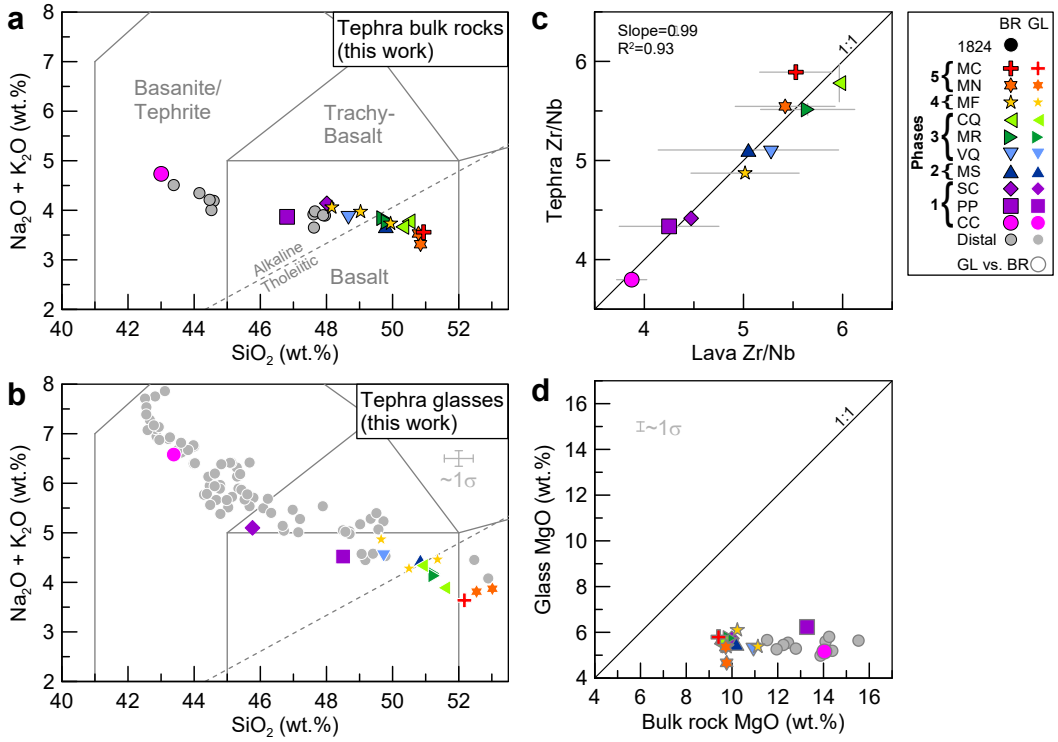

Figure 6. Tephra composition. TAS diagrams are shown for (a) bulk rocks and (b) matrix glasses of vent tephras and representative distal tephras, revealing the alkaline character of the majority of distal tephras. Each data point represents 1–7 EPMA analyses. The gray cross labelled ~1σ in (b) indicates the average standard deviation of multiple analyses within a single sample. (c) Comparison of the Zr/Nb ratios of vent tephras (this work) with that of lavas reported by Carracedo et al. (1990), showing excellent correspondence. Error bars are one standard deviation of the mean of multiple analyses. (d) Comparison of the MgO content of matrix glasses with that of corresponding bulk rocks for our tephra samples, showing a large discrepancy due to the olivine-rich crystal cargo of Timanfaya tephras. Error bar as in (b). Sample type: BR: bulk rock; GL: matrix glass. Sample identification: CC: Caldera de los Cuervos; PP: Pico Partido; SC: Caldera de Santa Catalina; MS: Montañas del Señalo; VQ: Volcán El Quemado; MR: Montaña Rajada; CQ: Calderas Quemadas; MF: Montañas del Fuego; MN: Montaña de las Nueces; MC: Montaña Colorada (see Figure 1); 1824: 1824 eruption; distal: distal tephras from stratigraphic sections.

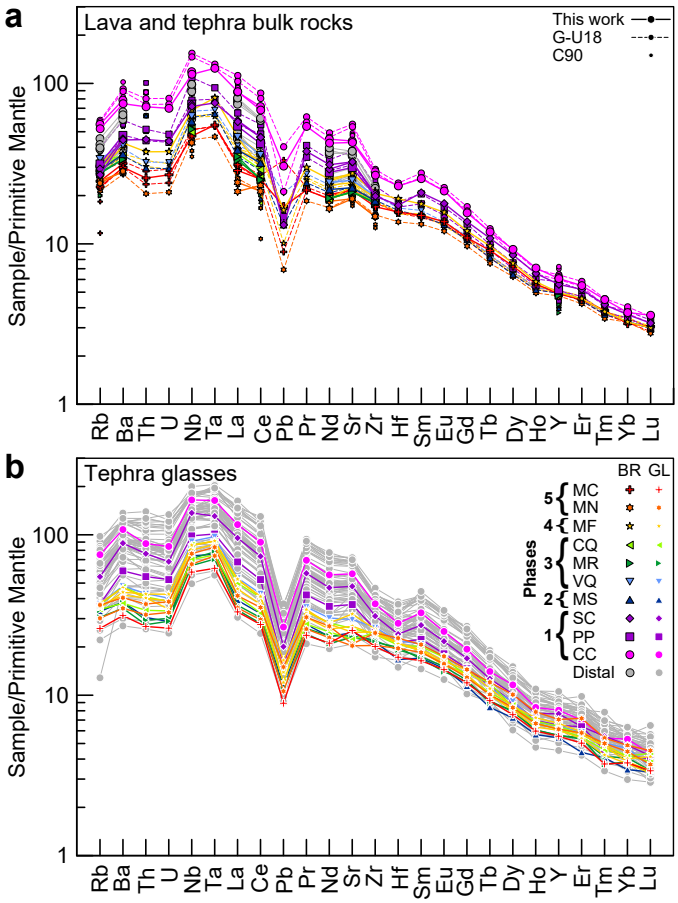

Figure 7. Primitive mantle-normalized multi-element diagrams. (a) Comparison of bulk rock samples from Gómez-Ulla et al. (2018) (G-U18) and Carracedo et al. (1990) (C90) and this work. Th and U values obtained by XRF were omitted due to low precision. (b) Matrix glass data for both vent (colored lines) and distal (gray lines) tephras, showing the enriched nature of distal tephras resembling the compositions of Caldera de los Cuervos (CC), Pico Partido (PP) and Caldera de Santa Catalina (SC) tephras. Most distal tephras also show negative Zr and Hf anomalies. Primitive mantle values are those of McDonough and Sun (1995). Legends apply to both panels, with symbols, color code and abbreviations as in Figure 6.

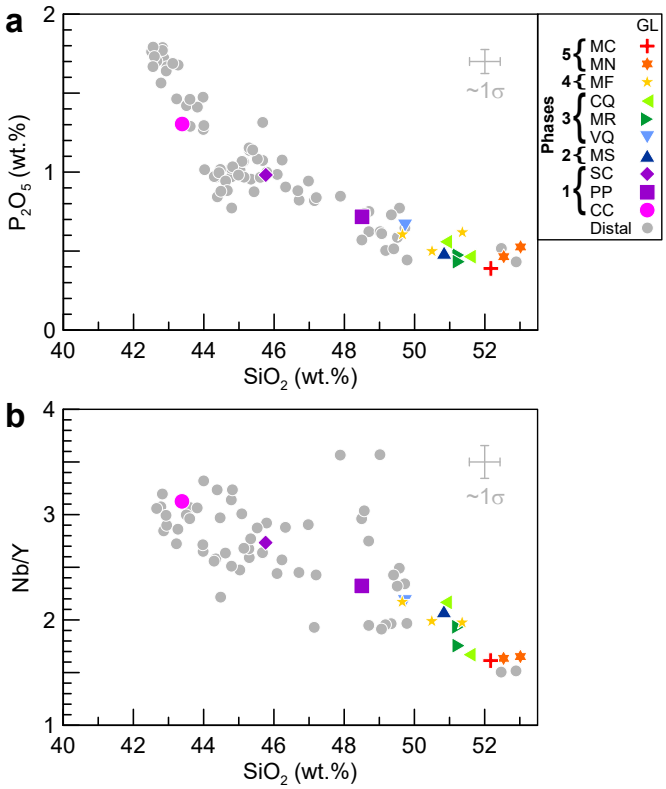

Figure 8. Distal tephra–source vent correlation plots. (a) P_2O_5 and (b) Nb/Y against SiO_2 content for distal and vent tephra glasses. Distal tephras are matched to their corresponding source vent based on Euclidean distance minima (Table S5). Gray crosses labelled ~1σ indicates the average intra-sample standard deviation. Legend applies to both panels, with symbols, color code and abbreviations as in Figure 6.

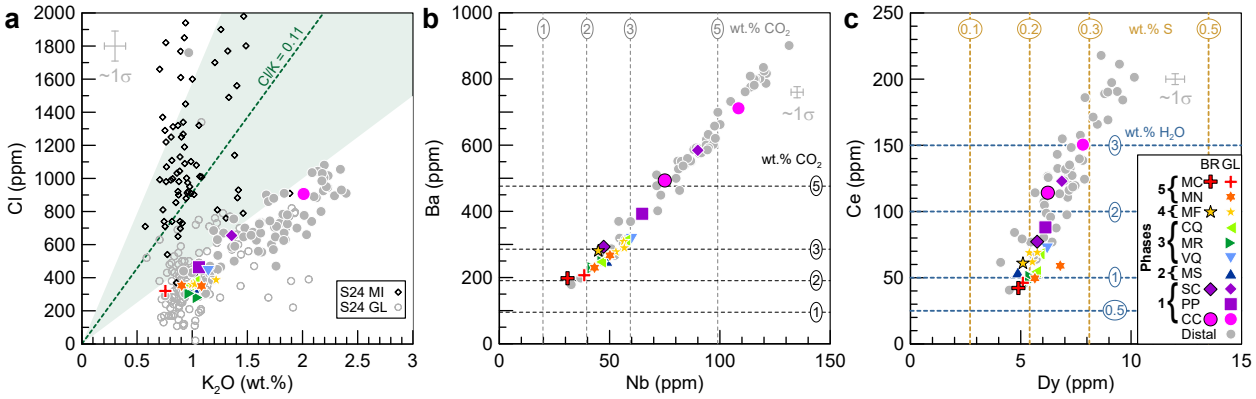

Figure 9. Volatiles and trace element proxies. (a) Cl and K_2O contents in our Timanfaya matrix glasses compared to the data of Sharma et al. (2024) (S24) for melt inclusions (MI, open black diamonds) and matrix glasses (GL, open gray circles). Matrix glasses show Cl/K ratios that are lower than the Primitive Mantle value of 0.11 (with a one standard deviation range of 0.06–0.19 shown by the shaded green envelope) proposed by Palme and O'Neill (2003), whereas melt inclusions largely fall close to, or above, it. This indicates substantial syn-eruptive chlorine degassing during the Timanfaya eruption. (b) Ba and Nb concentrations as proxies for undegassed CO_2 content. (LA-)ICP-MS data only. Horizontal and vertical dashed lines denote predicted CO_2 contents (circled numbers, in wt.%) assuming mantle CO_2/Ba and CO_2/Nb ratios of 105 (Michael & Graham, 2015) and 505 (Rosenthal et al., 2015), respectively. (c) Ce and Dy concentrations as proxies for undegassed H_2O and S contents, respectively. (LA-)ICP-MS data only. Predicted H_2O contents based on a H_2O/Ce ratio of 200 (Michael, 1995; Saal et al., 2002) are shown by horizontal dashed lines, whereas vertical dashed lines mark predicted S concentrations using a S/Dy ratio of 370 (McDonough & Sun, 1995). Gray crosses labelled ~1σ indicates the average intra-sample standard deviation. Legend in (c) applies to all panels, with symbols, color code and abbreviations as in Figure 6.

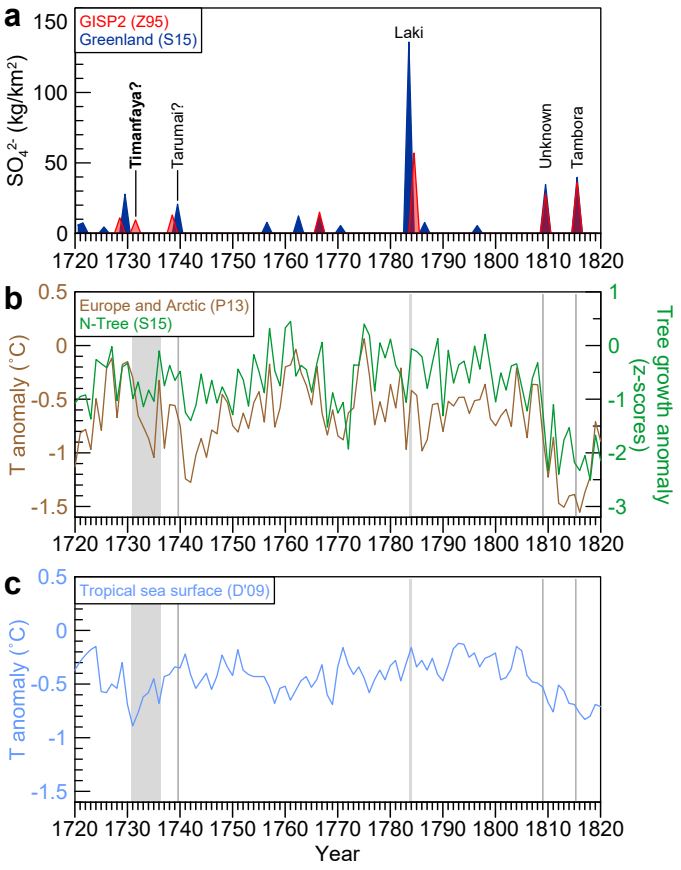

Figure 10. Paleoclimate records. (a) Sulfate anomalies in the Greenland ice sheet, from a single (Zielinski, 1995; Z95, red) and multiple ice cores (Sigl et al., 2015; S15, navy blue). Peaks associated with the 1815 CE Tambora eruption, 1809 CE unknown, and 1783–1784 CE Laki eruptions are labelled, along with anomalies possibly related to the 1739 CE VEI 5 eruption of Tarumai, Japan (Toohey & Sigl, 2017), and the 1730–1736 CE Timanfaya eruption. (b) Temperature anomaly for Europe and the Arctic (PAGES 2k Consortium, 2013; P13, brown) with respect to the 1961–1990 average and tree-ring growth anomalies relative to the 1000–1099 CE period from a Northern Hemisphere data composite (Sigl et al., 2015; S15, green). (c) Tropical sea surface temperature anomalies, with respect to the 1897–1981 period, from a multi-proxy reconstruction (D'Arrigo et al., 2009; D'09, light blue). The gray lines in panels (b) and (c) show the durations of the eruptions labelled in (a).